

Nano carbon dust emission in proto-planetary disks: the aliphatic-aromatic components

T. Boutéraon¹, E. Habart¹, N. Ysard¹, A.P. Jones¹, E. Dartois², T. Pino²

¹Institut d'Astrophysique Spatiale (IAS), UMR 8617-CNRS Université Paris Sud, 91405 Orsay, France

²Institut des Sciences Moléculaires d'Orsay (ISMO), CNRS, Univ Paris Sud, Université Paris-Saclay, 91405 Orsay, France
e-mail: thomas.bouteraon@ias.u-psud.fr

Preprint online version: January 22, 2019

ABSTRACT

Context. In the interstellar medium, carbon (nano-)grains are a major component of interstellar dust. This solid phase is more vulnerable to processing and destruction than its silicate counterpart. It exhibits a complex, size-dependent evolution due to interactions within different radiative and dynamical environments. Infrared signatures of these nanocarbon grains are seen in a large number of disks around Herbig HAeBe stars.

Aims. We probe the composition and evolution of carbon nano-grains at the surface of (pre-)transitional protoplanetary disks around Herbig stars.

Methods. We present spatially resolved infrared emission spectra obtained with NAOS CONICA at the VLT in the 3–4 μm range with a spatial resolution of 0.1", which allow us to trace aromatic, olefinic and aliphatic bands which are attributed to sub-nanometer hydrocarbon grains. We apply a gaussian fitting to analyse the observed spectral signatures. Finally, we propose an interpretation in the framework of the The Heterogeneous dust Evolution Model of Interstellar Solids (THEMIS).

Results. We show the presence of several spatially extended spectral features, related to aromatic and aliphatic hydrocarbon material in disks around Herbig stars, from ~ 10 to 50–100 au, and even in inner gaps devoided of large grains. The correlation and constant intensity ratios between aliphatic and aromatic CH stretching bands suggest a common nature of the carriers. Given their expected high destruction rates due to UV photons, our observations suggest that they are continuously replenished at the disk surfaces.

Key words. proto-planetary disk - carbonaceous dust - IR emission

1. Introduction

Carbonaceous dust is a major component of the solid matter present in the interstellar medium (ISM). It is observed in a wide variety of environments, both in emission and extinction. Much more sensitive to energetic events than its silicate counterpart, carbonaceous dust has been shown to be highly processed in UV irradiated regions and in shocks (e.g. Jones 1990; Dartois et al. 2004b,a; Pino et al. 2008; Mennella 2008; Godard et al. 2011; Micelotta et al. 2010b,a). It is thus expected to be sensitive to the local physical conditions in the environments where it is observed. Processing of carbonaceous dust is expected to be reflected in the aromatic and aliphatic near- to mid-IR emission bands that are attributed to sub-nanometers polycyclic aromatic hydrocarbon-like molecules (PAHs) (Leger & Puget 1984) or hydrogenated amorphous carbons (a-C:H) (Jones 1990, and references therein). a-C(:H), including both H-poor a-C and H-rich a-c:H, materials are a broad family of compounds including various proportion of polyaromatic units, of various sizes, linked by olefinic and aliphatic bridges. This component, when observed in emission, associated with the aromatic phase, should thus exhibit a series of bands between 3.4 and 3.6 μm , in addition to the aromatic 3.3 μm band (e.g., Geballe et al. 1985; Jourdain de Muizon et al. 1990b,a; Joblin et al. 1996; Goto et al. 2003; Pilleri et al. 2015), as well as, bands at 6.9 and 7.3 μm (Pino et al. 2008; Carpentier et al. 2012).

Aromatic Infrared Bands (AIBs) have been observed using ISO, Spitzer, AKARI and ground-based observations towards proto-planetary disks around pre-main-sequence stars (e.g., Brooke et al. 1993; Meeus et al. 2001; Acke & van den Ancker 2004; Habart et al. 2004; Sloan et al. 2005; Geers et al. 2006, 2007a,b; Keller et al. 2008; Acke et al. 2010; Maaskant et al. 2014; Seok & Li 2017). Based on Spitzer data, the detection rate is of $\sim 70\%$ in Herbig Ae stars, $\sim 50\%$ in Herbig Be stars (Acke et al. 2010), and $\sim 10\%$ in T Tauri stars (Furlan et al. 2006; Geers et al. 2006). AIBs are detected only towards a few debris disks (Chen et al. 2006a). Furthermore, mid-IR bands attributed to C-H aliphatic bonds at 6.9 and 7.3 μm have been observed in $\sim 55\%$ of Herbig stars (Acke et al. 2010). The study of the aromatic/aliphatic band ratio in the mid-IR Spitzer spectra (Acke et al. 2010) suggests that strong UV fluxes reduce the aliphatic component and magnify the spectral signature of the aromatic molecules in the IR spectra. However, dehydrogenation caused by UV photons (Muñoz Caro et al. 2001) also reduces C-H aromatic signatures. Finally, fullerenes have been detected in one disk (Roberts et al. 2012).

Bands between 3.4 and 3.6 μm have also been detected in some Herbig Ae/Be (HAeBe) stars (e.g., Acke & Van den Ancker 2006; Habart et al. 2006). Few of them (2 to 3) show peculiar strong features that peak at 3.43 and 3.53 μm (e.g., Blades & Whittet 1980; Guillois et al. 1999; Van Kerckhoven et al. 2002). Using adaptative optics high angular resolution spectroscopic observations of the HAeBe star HD 97048 and Elias 1, the

emission in the strong features at 3.43 and 3.53 μm was spatially resolved (Habart et al. 2004; Goto et al. 2009). Several studies have proposed attributing these features to surface C-H stretching modes on 10-50 nm or larger diamond particles (e.g., Guillois et al. 1999; Sheu et al. 2002; Jones et al. 2004; Pirali et al. 2007). On the other hand, some disks show relatively weak but distinguishable features between 3.4 and 3.6 μm at 3.40, 3.46, 3.51, and 3.56 μm (e.g. Sloan et al. 1997)(e.g. Sloan et al 1997) which may be attributed to aliphatic components. These features were also detected towards Photo-Dissociation Regions (PDRs) in star forming regions, reflection nebulae and (proto)planetary nebulae (e.g., Geballe et al. 1985; Jourdain de Muizon et al. 1990b,a; Joblin et al. 1996; Goto et al. 2003; Pilleri et al. 2015). Toward a proto-planetary nebula, Goto et al. (2003) found that the relative intensity of the aliphatic feature at 3.4 μm to the aromatic feature at 3.3 μm decreases with the distance from the star. They suggested that thermal processing is likely to account for the spectral variation, reflecting the history of the planetary nebula. Towards the NGC 7023 North West PDR, Pilleri et al. (2015) traced the evolution of the 3.3 and 3.4 μm bands. They showed that the intensity of the 3.3 μm band relative to the total PAH emission increases with the UV flux, while the relative contribution of the 3.4 μm band decreases with the UV flux. The UV photo-processing of Very Small Grains leading to PAHs with attached aliphatic sidegroups in the lower UV flux region, and then becoming PAHs in the higher UV flux region was suggested to explain the spectral variation. Variations in the ratio of the 3.3 to 3.4 micron bands raise the question of the nature and stability of the carriers of these bands and of their excitation mechanisms as a function of the local physical conditions.

Studying the aromatic and aliphatic bands in proto-planetary disks, where the carbon nano-grains are likely highly processed, is thus important to understand the mechanisms at work on carbon dust. Photo-induced processes may be important at the disk surfaces. Carbon nano-grains, that escape settling, are very well coupled to the gas in the upper disk layers. The AIBs emission arises from the very thin upper disk surface layers where UV photons from the central star penetrate, which can be interpreted as a PDR. Because of the stochastic heating mechanism, the emission in the bands is spatially extended (Habart et al. 2006, e.g.) and thus makes it possible to probe the composition of the disk surface material over large distances, as well as, the geometry of the disks. High AIBs-to-stellar luminosity ratios are observed in targets with a flared disk (e.g., Meeus et al. 2001; Habart et al. 2004; Keller et al. 2008; Acke et al. 2010). Observations of AIBs provide one of the most striking indications for flared disks around HAeBe stars (e.g., Lagage et al. 2006; Berné et al. 2015). Furthermore, AIBs have been detected in the inner disk cavities, where on-going planet formation could have started (e.g., Geers et al. 2007a; Maaskant et al. 2013, 2014; Kraus et al. 2013; Schworer et al. 2017). Recently, near-IR interferometric observations of HAeBe stars tracing the inner part of the warm dusty disks revealed unusually extended NIR emission (out to ~ 10 AU Klarmann et al. 2017; Kluska et al. 2018). This suggests the presence of stochastically heated very small (sub-)nanometer grains in the inner disk parts. Finally, carbon nano-grains could play, as in PDRs, a key role in gas heating via the photoelectric effect and, thus influence the disk vertical structure (e.g., Meeus et al. 2012). Due to their very large effective surface area, nano-grains are also expected to have an important role in the formation of key molecules (e.g., H_2 , hydrocarbon molecules) and charge balance. Hence, a better knowledge of them is essential to understand the disk physics and chemistry.

This study focuses on the near-IR emission between 3 and 4 μm of spatially resolved spectra around young Herbig stars orbited by a proto-planetary disk and observed with the NAOS CONICA (NACO) instrument at the Very Large Telescope (VLT) in Chile. This is the first spatially resolved study of the weak bands in the 3 to 4 μm -range in protoplanetary disks. Our aim is to use the aromatic and aliphatic signatures detected at the disk surfaces to characterise the size and composition of the sub-nanometer carbonaceous grains. In section 2, we discuss the diversity of the carbonaceous signatures. In section 3, we give the astrophysical parameters and the main characteristics of the observed disks. In section 4, we describe the observations and data reduction. In section 5, we present the observational results, the spectral signatures fitting method and the identified bands. In section 6, we briefly describe the THEMIS framework, a global model, in which dust composition, evolution and signatures can be analysed. In section 7, we discuss the results and their astrophysical implications.

2. The variability of the carbonaceous signatures

Fig. 1 presents the diversity of features related to hydrogenated amorphous carbonaceous (a-C:H) materials in the 3-4 μm near-infrared (IR) range where C-H stretching vibrational modes are observed. These vibrational modes are particularly interesting since they characterise bonds between carbon and hydrogen atoms varying according to their local environment (closest neighbours).

Fig. 1 illustrates these variations for the related signatures of two major types of laboratory experiments. Four experiments concern a-C:H deposited on thin film samples (Dartois et al. 2005, 2004b; Ristein 1998; Dischler 1987) and one experiment focuses on soot nano-particles, having disordered carbon nano-structurations, produced in flames (Pino et al. 2008). Analysis had been made using IR absorption spectroscopy. The experiments of these studies give an overview of the variability of the features related to carbonaceous materials and highlight the difficulty of signature assignments. It should be noticed that the band origin assignment in the 3.22 - 3.32 μm range is still quite uncertain due to the presence of four or five overlapping vibrations in this region.

Table 1 gives assumed signature assignments, their band centre and width ranges, both in wavelengths and wavenumbers. These modes correspond to C-H stretching (str) vibrational modes. We distinguish three main kinds of bonds: aromatics, olefinics, and aliphatics. Representation of such vibration modes are given in Fig. 1. The aromatic band at 3.3 μm corresponds to the vibration of hydrogen bonded to a carbon included in an aromatic cycle and labeled sp^2 (hybridization state) CH aromatic (aro.). Its band centre varies from 3.268 to 3.295 μm and its width from 0.005 to 0.057 μm . Olefinic (ole.) modes correspond to the vibration of CH or CH_2 group where the carbon atom is engaged in a C=C bond. The CH_2 asymmetric (asy) mode varies from 3.240 to 3.249 μm with a width between 0.014 and 0.045 μm . It is less variable than its symmetrical (sym) counterpart, for which the band centre varies from 3.350 to 3.396 μm and the width between 0.003 and 0.028 μm . A third olefinic mode involving only CH group occurs at an intermediate wavelength between 3.311 and 3.344 μm with width variations between 0.008 and 0.062 μm . These modes are related to a sp^2 planar hybridization, where one carbon atom forms bonds with three other atoms.

Two types of aliphatic (ali.) modes can be distinguished in the CH stretch region: those originated in the CH_3 and CH_2 func-

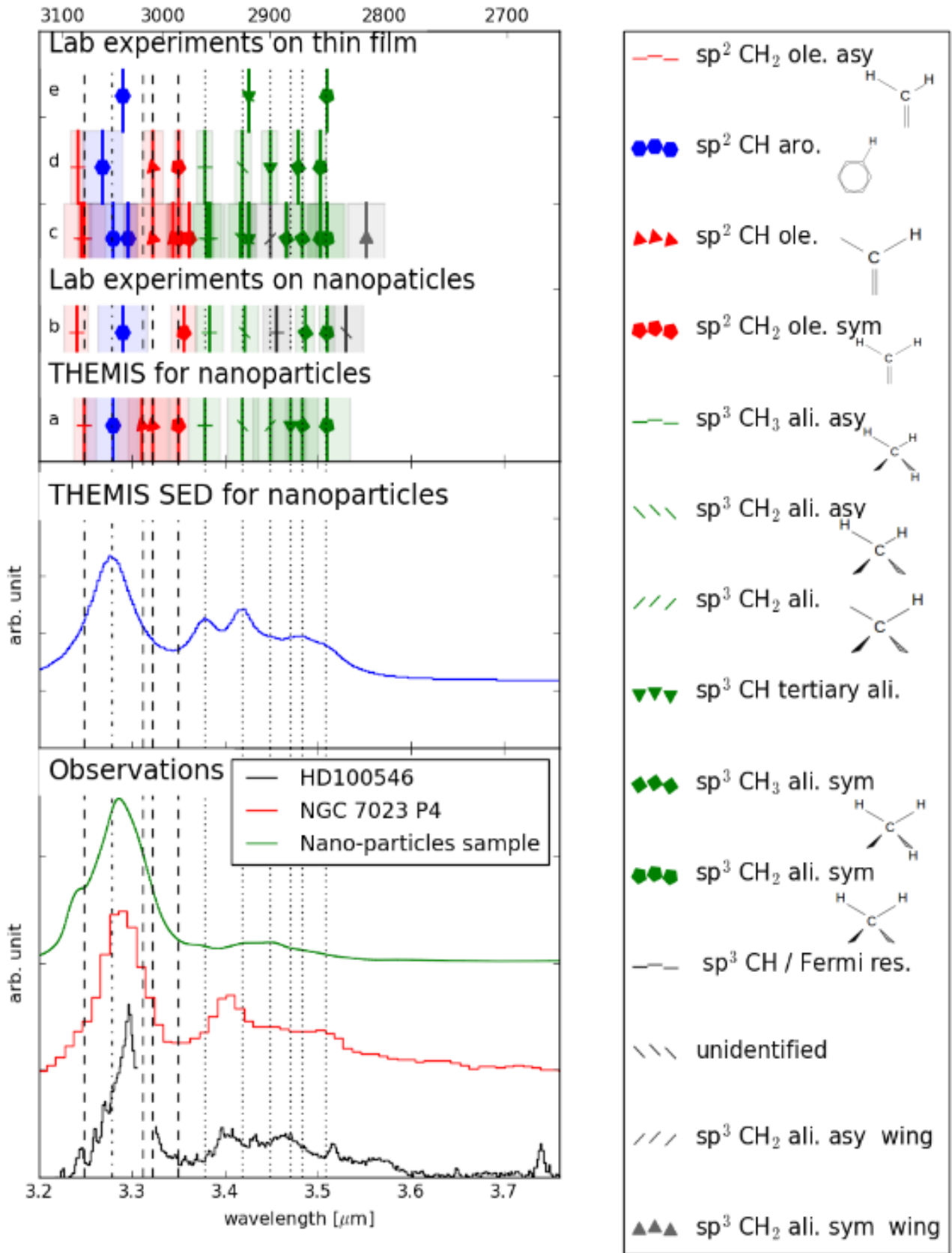


Fig. 1. Top panel shows the band centre (line) and width (transparent box) of the spectral signatures related to a-C:H materials obtained in laboratory experiments on thin film or on nanoparticles in the mid-IR range where C-H stretching vibrational modes are observed. In blue is shown the aromatic compound, in red olefinic bonds, in green aliphatic ones and in grey other non-assigned signatures. The signatures used in the THEMIS model are based on these experiments and are drawn in row *a* and are extended by vertical lines for aromatics (dash-dotted), olefinics (dashed), aliphatics (dotted). Middle panel shows the spectral energy distribution (SED) for an H-poor, aromatic-rich grain population from the THEMIS model and calculated with DustEM. The bottom panel shows characteristic spectrum from our study that shows the whole diversity observed in this range around the Herbig star HD 100546. Spectra from the PDR NGC 7023 (Pillari et al. 2015) and nano-particles (Carpentier et al. 2012) (related to the study of Pino et al. (2008)) are also plotted for the comparison. In the right panel, the signatures are labelled and a schematic view of vibrational modes is given. *a*: Jones et al. (2017), *b*: Pino et al. (2008), *c*: Dartois et al. (2004b), *d*: Dustem (1998), *e*: Discher (1987).

tional group, with their asymmetric and symmetric characters. The CH_3 aliph asym mode varies from 3.378 to 3.84 μm and its width between 0.008 and 0.033 μm , while the CH_2 aliph asym mode varies from 3.413 to 3.425 μm and its width between 0.006 and 0.034 μm . At longer wavelength, the CH_3 aliph sym mode varies from 3.466 to 3.486 μm and its width between 0.006 and 0.034 μm while the CH_2 aliph sym mode varies from 3.503 to 3.509 μm and its width between 0.006 and 0.051 μm . A fifth mode related to the aliphatic CH can be found at an intermediate wavelength between symmetric and asymmetric modes. It is labeled as tertiary and its band centre varies from 3.425 to 3.47 μm and its width between 0.006 and 0.036 μm . All aliphatic modes have a sp^3 hybridization in which carbon atoms are bonded to four other atoms.

In the following, observational data will be compared to the THEMIS model (Jones et al. 2017, 2013), which takes into account vibrational modes coming from the thin film experiments described above. The bands included in THEMIS (assignment and characteristics) are also plotted in Fig. 1 for comparison. A typical spectrum from the disk observation and one from the PDR NGC 7023 (Pilleri et al. 2015) are also plotted for comparison. Obvious differences between lab data, observations, and the model are found, which will be discussed in Sect. 6.

3. Selected (pre-)transitional disks

Our sample consists of four well-known Herbig Ae/Be stars, all with evidence of a circumstellar disk thought to be in transition from a gas-rich proto-planetary disk to a gas-depleted debris disk. The four disks show clear evidence of flaring from their spectral energy distribution modelling (Meeus et al. (2001)), and IR and millimeter interferometry observations (detailed descriptions of the disks and the associated references are given in Appendix A). Furthermore, it has recently become clear that these four disks show many spatial structures, such as annular gaps and rings in the large grain emission distribution near the mid-plane as seen in millimeter and in the near-IR stellar scattered light by μm grains. Large scale spiral arms are also seen in scattered light. In the innermost few astronomical units (AU), evidence for a radial gap separating an inner disk (from ~ 0.1 to few AU) and the outer main disk (from ~ 10 to 100 AU or more) was found using near- and mid-IR observations. Some of these structures could be tracing on-going planet formation. Planet candidates have been found around two of our disks: HD 100546 (e.g., Quanz et al. 2015; Currie et al. 2015) and HD 169142 (Biller et al. 2014; Reggiani et al. 2014; Osorio et al. 2014). However, as discussed by several authors, the observed disk structures could also result from gravitational perturbations by binary stars, disk dynamical evolution (e.g., gas accretion from the surrounding molecular cloud, local maximum pressure) or dust evolution.

These disks have been observed at different wavelengths, using ISO, Spitzer and ground-based spectroscopy, all showing aromatic emission features and possible aliphatic emission features (Meeus et al. 2001; Acke & van den Ancker 2004; Sloan et al. 2005; Habart et al. 2006; Geers et al. 2007b; Keller et al. 2008; Acke et al. 2010; Seok & Li 2017). In Table 2, we report (i) the astrophysical parameters of each star (spectral type, effective temperature, luminosity, mass, age, distance, and G_0 , i.e., far-ultraviolet (FUV) flux strength at 50 AU from the star in terms of the Habing field (Habing 1968), and (ii) the dust spectral characteristics (presence of aromatic and aliphatic). We also give the strength of the 3.3 μm aromatic emission feature measured from the ISO spectra of Meeus et al. (2001); Van Kerckhoven et al. (2002). Estimations of the radial spatial extension of the

3.3 μm aromatic emission feature (full-width at half-maximum, FWHM) measured from ground-based spatially resolved observations are also reported.

4. Observations and data reduction

Observations were performed using a long slit in the L-band, between 3.20 and 3.76 μm with the adaptive optics system NAOS-CONICA (NACO) at the VLT. The on sky projection of the slit is 28"-long and 0.086"-wide that corresponds to the diffraction limit in this wavelength range. The pixel scale is 0.0547" and the spectral resolution is $R = \lambda / \Delta \lambda \sim 1000$. We took several slit positions, one centred on the star and the other slits shifted by a half width. Seven or nine positions allowed to extract spectra on an area star-centred of 2"x0.258" or 2"x0.354", respectively. The long slit was aligned in the north-south direction, except for HD 100546. For HD 100546, the long slit was aligned with the major axis of the disk as resolved in scattered light (Augereau et al. 2001; Grady et al. 2001) with a position angle of ~ 160 degrees measured east of north. The integration time per slit was 3 minutes. The data set reference is 075.C-0624(A) and observations characteristics are summarised in Table 2.

Ground-based near-IR spectroscopic observations involve the use of a standard procedure to subtract the atmospheric contribution. For each disk, we employed the standard chopping/nodding technique with a throw of $\sim 9''$ in the north-south direction in order to correct from the atmospheric and instrumental background. Telluric bands due to the atmosphere were used for the wavelength calibration of spectra. They were removed using standard stars observed during each data set acquisition. To compensate for the airmass variation between the observations of the disk and the standard star, a scaling factor was applied to the standard star spectrum to optimize telluric band subtraction.

5. Results

5.1. Extraction, decomposition and characteristic of the spectra

For the four disks, spectra were extracted from pixels for each slit on both sides of the central star, covering an area of 2"x0.258" or 2"x0.354" star-centred. Since we aim to focus on the carbonaceous dust emission evolution we extract the features from the original data by subtracting an underlying continuum. The continuum is subtracted with a polynomial of order three considering ranges where bands are absent, i.e. 3.6 - 3.7 μm range, and 3.2 μm . The intensity at 3.35 μm was used to constrain the polynomial so that the continuum is not higher than the signal. The spectra show similar structures for the four disks: the 3.3 μm aromatic feature, at least five features between 3.4 and 3.6 μm (cf Fig. 3), and hydrogen recombination lines Pfund 9 and 8 at 3.297 and 3.741 μm .

To interpret the shape and the evolution of the features moving away from the central star, we consider a heterogeneous widening assuming the presence of several carriers associated with the same signature and make a Gaussian decomposition of the spectra based on the experiments discussed in Sect. 2. The size, temperature, structure, and even composition of the various carriers imply that the signature is composed of multiple components. A good approximation of these signatures is thus a series of gaussian profiles. We use eight Gaussians:

- 3.3 μm : related to the C-H stretching mode of aromatics
- 3.4, 3.43, 3.46, 3.52, and 3.56 μm most probably associated with aliphatic materials.

Table 1. Band centre (λ_0 , ν_0) and full width at half maximum (FWHM) variations in laboratory experiments.

band	λ_0 [μm]	FWHM [μm]	ν_0 [cm^{-1}]	FWHM [cm^{-1}]
sp ² CH ₂ ole. asy str	3.240 - 3.249	0.014 - 0.045	3089 - 3078	13.3 - 42.4
sp ² CH aro	3.268 - 3.295	0.005 - 0.057	3060 - 3035	5 - 53.1
sp ² CH ole.	3.311 - 3.344	0.008 - 0.062	2990 - 3020	7 - 56.3
sp ² CH ₂ ole. sym str	3.350 - 3.396	0.003 - 0.028	2985 - 2945	3 - 25
sp ² CH ₃ ali. asy str	3.378 - 3.384	0.008 - 0.033	2960 - 2955	7 - 29.3
sp ³ CH ₂ ali. asy str	3.413 - 3.425	0.006 - 0.034	2930 - 2920	5 - 28.9
sp ³ CH tertiary ali. / Fermi resonance	3.425 - 3.47	0.006 - 0.036	2920 - 2882	5 - 30
sp ³ CH ₃ ali. sym str	3.466 - 3.486	0.006 - 0.034	2885 - 2869	5 - 27.8
sp ³ CH ₂ ali. sym str	3.503 - 3.509	0.006 - 0.051	2855 - 2850	5 - 41.8
sp ³ CH ₂ ali. sym str wing	3.552	0.039 - 0.068	2815	31 - 53.6

Table 2. Top part: Astrophysical parameters of the selected disks. The standard star used for data reduction is HR6572. Spectral type, effective temperature, luminosity, mass, age (Seok & Li 2017). Distance (Gaia Collaboration et al. 2018). G_0 : far-ultraviolet (FUV) flux strength at 50 AU from the star expressed in units of the average interstellar radiation field, $1.6 \times 10^{-3} \text{ erg s}^{-1} \text{ cm}^{-2}$ (Habing 1968). Integrated strength of the aromatic 3.3 μm feature (Habart et al. 2004). Estimation of the radial spatial extension of the 3.3 μm band (full width at half-maximum, FWHM) for HD 100546, HD 100453 and HD 169142 (Geers et al. 2007b; Habart et al. 2006). FWHM for HD 17918 (this work) Bottom part: Summary of the observations. SR, Strehl ratio or coherent energy. r_0 , Fried parameter. L_0 , outer scale.

	HD 100546	HD 100453	HD 169142	HD 179218
Spec. type	B9Vne	A9Ve	B9V	A0Ve
Temp. [K]	10500	7600	8250	9640
Lum. [L_\odot]	32	10	8.55	182
M [M_\odot]	2.4	1.8	1.69	3.66
Age [Myr]	> 10	15 (10 ?)	6	1.08
d [pc]	109	104	117	245
G_0 at 50 AU	4.2×10^6	2.4×10^5	3.4×10^5	1.6×10^7
$I_{3.3}$ [10^{-14} W/m^2]	2.5 ± 0.5	1.3 ± 0.2	1 ± 0.2	1.7 ± 0.2
FWHM [AU]	12 (up to 50)	20	43	35
Date	2005/03/26	2005/03/30	2005/05/05	2005/07/14
Airmass	1.56	1.17	1.01	1.32
SR [%]	46	38	37	53
r_0 [cm]	16	8	11	14
L_0 [m]	25	19	18	17
Seeing ["]	0.66	1.17	0.93	0.69

Table 3. Initial parameters of the gaussian decomposition method.

Feature	Band centre [cm^{-1}]	Standard deviation [cm^{-1}]
3.3 μm	3040 ± 10	25 ± 10
3.4 μm	2941 ± 10	15 ± 5
3.43 μm	2915 ± 10	10 ± 5
3.46 μm	2890 ± 10	15 ± 5
3.52 μm	2841 ± 10	15 ± 5
3.56 μm	2809 ± 10	20 ± 10
H Pfund 9	3027 ± 5	2.25 ± 0.3
H Pfund 8	2667 ± 5	2.25 ± 0.3

– 3.297 and 3.741 μm which are the recombination lines Pfund 9 and 8 of hydrogen.

The decomposition is made on the continuum subtracted spectra expressed in wavenumber. The initial parameters and their tolerance range are summarised in Table 3. A zoom of the decomposition is presented in Fig. 3.

We optimize the parameters for each Gaussian using the Powell method. If the amplitude of the 3.3 μm band is three times lower than the mean noise of the underlying continuum, the spectrum is excluded. Then, we average the spectra according to their distance from the star, considering a step of 0.1"

corresponding to the spatial resolution of the instrument. Fig. 2 presents the characteristic spectra according to the distance to the central star. These are normalised to the continuum at 3.2 μm and thus show the evolution of the signatures relative to the continuum.

The main observation is that all the disks exhibit similar spectral signatures: a 3.3 μm aromatic feature, and other features in the 3.4 - 3.6 μm range 2.

Figure 3 shows details for one characteristic spectrum. For the 3.3, 3.4, and 3.46 μm , the FWHM are similar whereas for the 3.43 and 3.52 μm bands, they are narrower. The FWHM of the 3.56 μm band is broader but the feature is poorly fitted. Hydrogen Pfund recombination lines are very close to their theoretical values, 3.297 and 3.741 μm with a narrow FWHM and confirm the good wavelength calibration of the data. The decomposition method gives similar results for the other spectra.

In the following, we will focus on similarities and variations of these signatures.

5.2. Detection of the bands towards the disk

Aromatic and aliphatic bands are detected in HD 100546 between 0.2 and 0.9" (20-100 AU) in the main outer disk (see Fig. 2). In HD 100453, they are seen between 0.1 and 0.4" (10-40

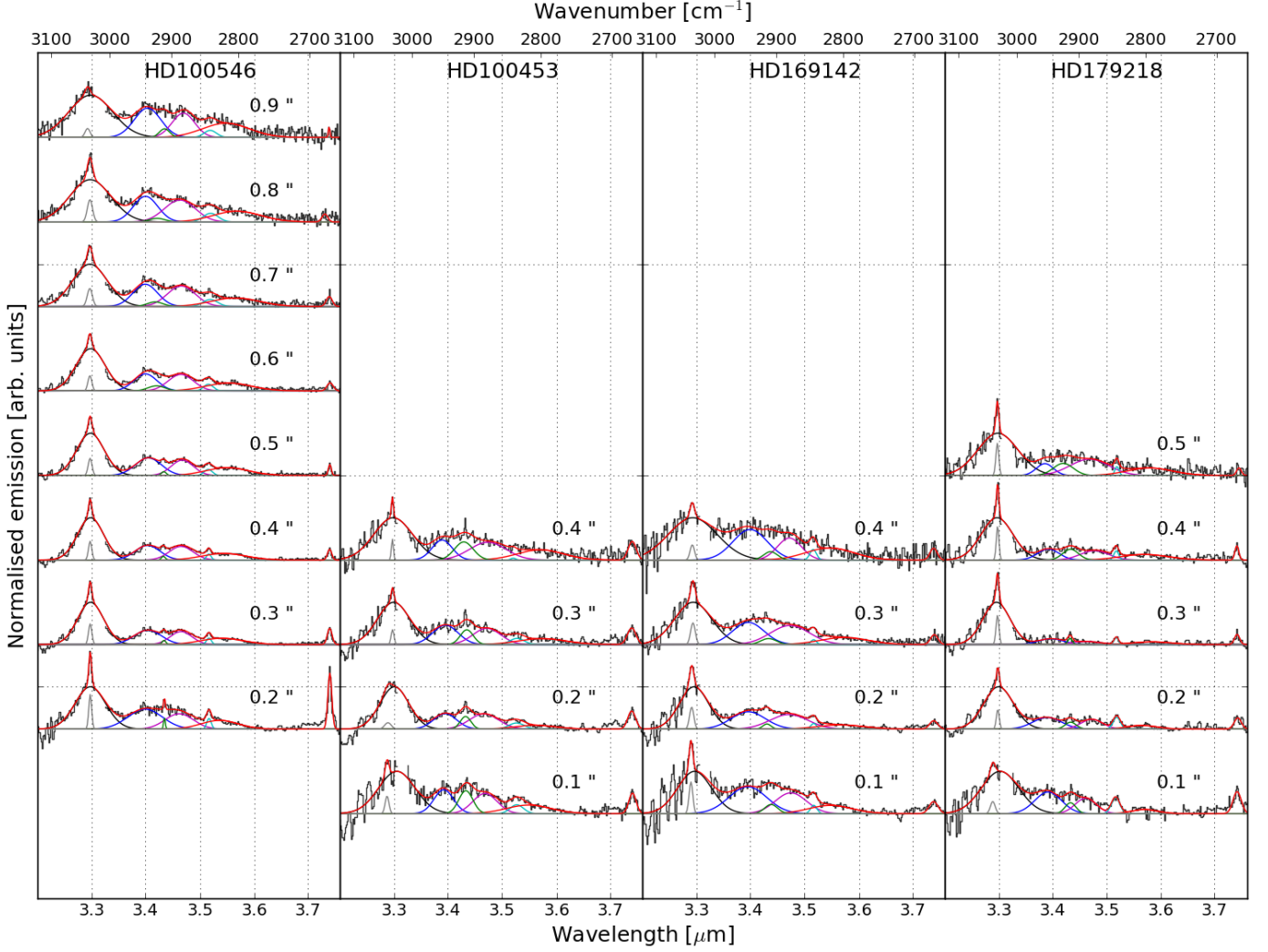


Fig. 2. NACO spectra averaged (in black) for different distances from the star in 0.1" step. Gaussian decomposition (in red) for each spectrum. Spectra are normalised to the continuum at 3.2 μm

AU) covering an area including both the gap that extends up to 20 AU and the external disk. Likewise, in HD 169142, signatures are detected between 0.1 and 0.4" (10-45 AU) which includes part of the two gaps detected between 1 and 20 AU, and between 30 and 55 AU. In HD 179218, bands are detected between 0.1" and 0.5" (30-120 AU). A gap exists out to 10 AU. Data do not allow us to probe the inner part of the disk. Interestingly, for most of the disks, the IR band carriers seem to be present both in the main disk regions and also in the gaps contrary to big grains (see references in the Appendix A).

5.3. Intensity variations

For each disk, Fig. 4 shows the intensities of each a-C:H emission band between 3.4 and 3.6 μm as a function of the intensity in the 3.3 μm aromatic band. These values come from the decomposition results of the individual pixel spectra that meet the selection criteria discussed previously. For HD 100546, HD 100453, and HD 169142, the values are mostly linearly distributed. For HD 179218, the distribution is less clear. The Spearman rank correlation coefficients which describe the monotonic relationship between two variables show a good correlation between the 3.4 to 3.6 μm features and the 3.3 μm feature. The

emission in aromatic and aliphatic bands in this wavelength range is very sensitive to the size of the particles. Also, finding such a spatial correlation suggests that the band carriers are both stochastically heated and have a similar size distribution.

Figure 5 presents the distribution ratio values for the 3.4-3.6 μm signatures to the 3.3 μm band as a function of the distance from the star. For HD 100546, HD 100453 and HD 169142, the 3.4/3.3, 3.43/3.3, 3.46/3.3, and 3.52/3.3 ratios are of the same order and have a narrow dispersion without significant evolution as a function of the distance from the star, except for the ratio 3.43/3.3 for HD 100546 which has a larger dispersion. For HD 179218, the ratios are lower by ~ 1.4 . As specified in Table 2, HD 179218 is more luminous than the three other stars, we expect carbonaceous materials to be differently processed due to the very different physical conditions. The aliphatic bonds, more fragile than the aromatic rings, are expected to be the first to break under UV processing.

5.4. The 3.3 μm band

In this section, we investigate the position and width of the 3.3 μm feature. Previous studies have pointed out that the 3.3 μm feature is actually composed of two sub-bands: one peaking at

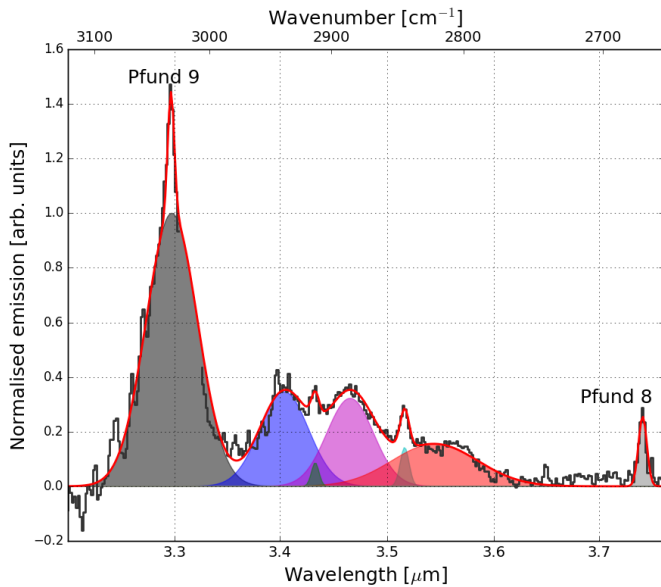


Fig. 3. NACO averaged spectrum (in black) of HD 100546 at 0.4" or 40 AU from the star. Gaussian decomposition is the red curve, hydrogen recombination lines are in grey. Individual contributor spectral signatures are identified at 3.3 μm (black), 3.4 μm (blue), 3.43 μm (green), 3.46 μm (magenta), 3.52 μm (cyan), 3.56 μm (red). The spectrum is normalised to the continuum at 3.2 μm .

3.28 μm and another at 3.30 μm (Sadjadi et al. 2017; Candian et al. 2012; Song et al. 2003; Tokunaga et al. 1991; Hammonds et al. 2015; Kwok & Zhang 2011). In particular, Tokunaga et al. (1991) classified the 3.3 μm band in two types. Type 1 peaking at 3.289 μm with width of 0.042 μm and observed in numerous objects such planetary nebulae and HII regions, a type 2, peaking at 3.296 μm with narrower width of 0.020 μm which are observed in pre-main sequence and evolved stars. Tokunaga et al. (1991) noted that laboratory data did not allow a particular assignment to the features and proposed that Type 2 are best fitted by amorphous aromatic materials and Type 1 by heated PAHs. As suggested in Fig. 5, the carriers of the bands are likely due to a single material. A series of studies made a distinction between Type 1 and Type 2 concerning the 3.3 μm band and investigated its origin in the Red Rectangle in emission (Song et al. 2003; Candian et al. 2012) and along a diffuse line of sight toward the Galactic centre (Chiar et al. 2013). While Candian et al. (2012) proposed that the 3.28 μm feature comes from the structural organisation of the PAHs, Chiar et al. (2013) suggested an aliphatic origin to the 3.28 μm band due the stretching mode of olefinic C-H bonds in amorphous hydrocarbons. Alternatively, Sadjadi et al. (2017) performed quantum mechanical calculations on a aromatic/aliphatic/olefinic compounds and proposed to assign the 3.28 μm feature to aromatics and the 3.30 μm to olefinics.

The averaged band centre and width of the 3.3 μm band and variations with distance from the star are given in Table 4. The band centre is in agreement with the laboratory experiments values reported in Table 1. For the all disks, the width, between 0.055 and 0.089 μm is globally higher than the highest width of 0.057 μm measured in the laboratory even if uncertainties could explain this difference in some cases. The averaged band centre and width of the other features and their variation ranges are given in Table 5.

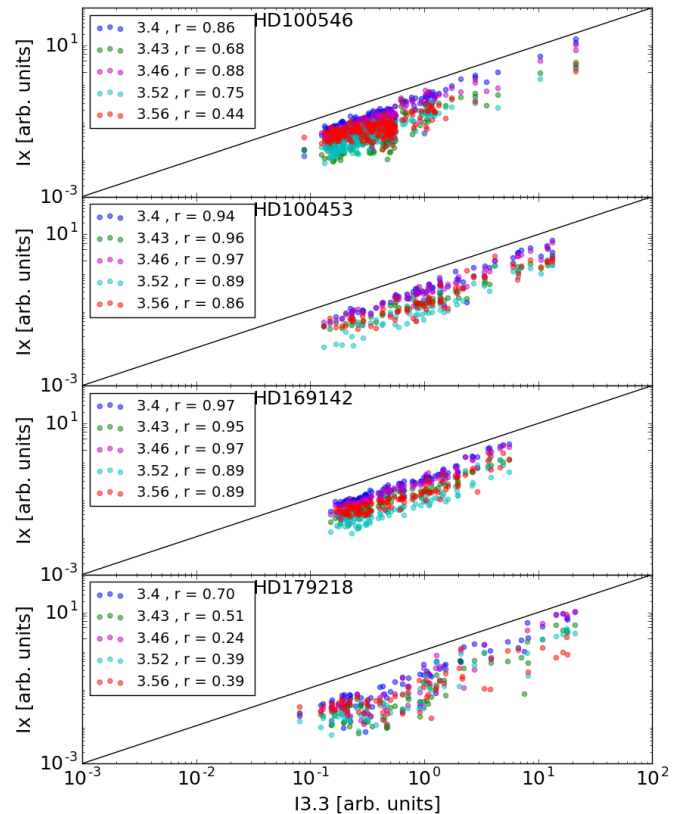


Fig. 4. Points are the intensity (amplitude $\times \sigma$) of 3.4 (blue), 3.43 (green), 3.46 (magenta), 3.52 (cyan), 3.56 (red) μm band as function of the 3.3 μm band intensity. For each set, the Spearman coefficient r is calculated.

In Fig. 6, the parameter values of the band centre and FWHM coming from the decomposition of pixel spectra are plotted as a function of the distance from the star. In the bottom panels, the FWHM is plotted versus to the band centre. The variations are reported in Table 4. In HD 100453 and HD 179218, the average band centre decreases with distance from 3.30 μm to 3.29 μm . In HD 100546 and HD 169142, the band centre remains constant at 3.295 μm moving away from the star. In all the disks, the FWHM decreases then increases with distance from the star. We also note that in HD 179218, the FWHM increases for band centres at longer wavelength. This suggests that close to 3.28 μm , the carrier of the feature would be more aromatic and around 3.30 or 3.32 μm , it would be more olefinic/aliphatic (Sadjadi et al. 2017; Chiar et al. 2013). In this case, a narrow width would mean that one component dominates when a broader one would represent the presence of both components. This aspect will be explored in more detail in Sect. 6. For HD 100453 and HD 179218, the 3.3 μm band centre seems to shift from higher to lower values with distance from the central star. A priori, this is unexpected given the known behaviour of carbonaceous materials irradiated by UV photons. Close from the star, we expect that amorphous aliphatic materials would be aromatised by the more intense UV photon flux (e.g., Jones 1990; Dartois et al. 2004b,a; Pino et al. 2008; Mennella 2008; Godard et al. 2011). Variations in the centre and width of the band suggest chemical processing (e.g. increasing contribution of olefinic/aliphatic bridges with increasing distance to the star) which are complex and difficult to interpret, requiring further study to allow definitive conclusions. The

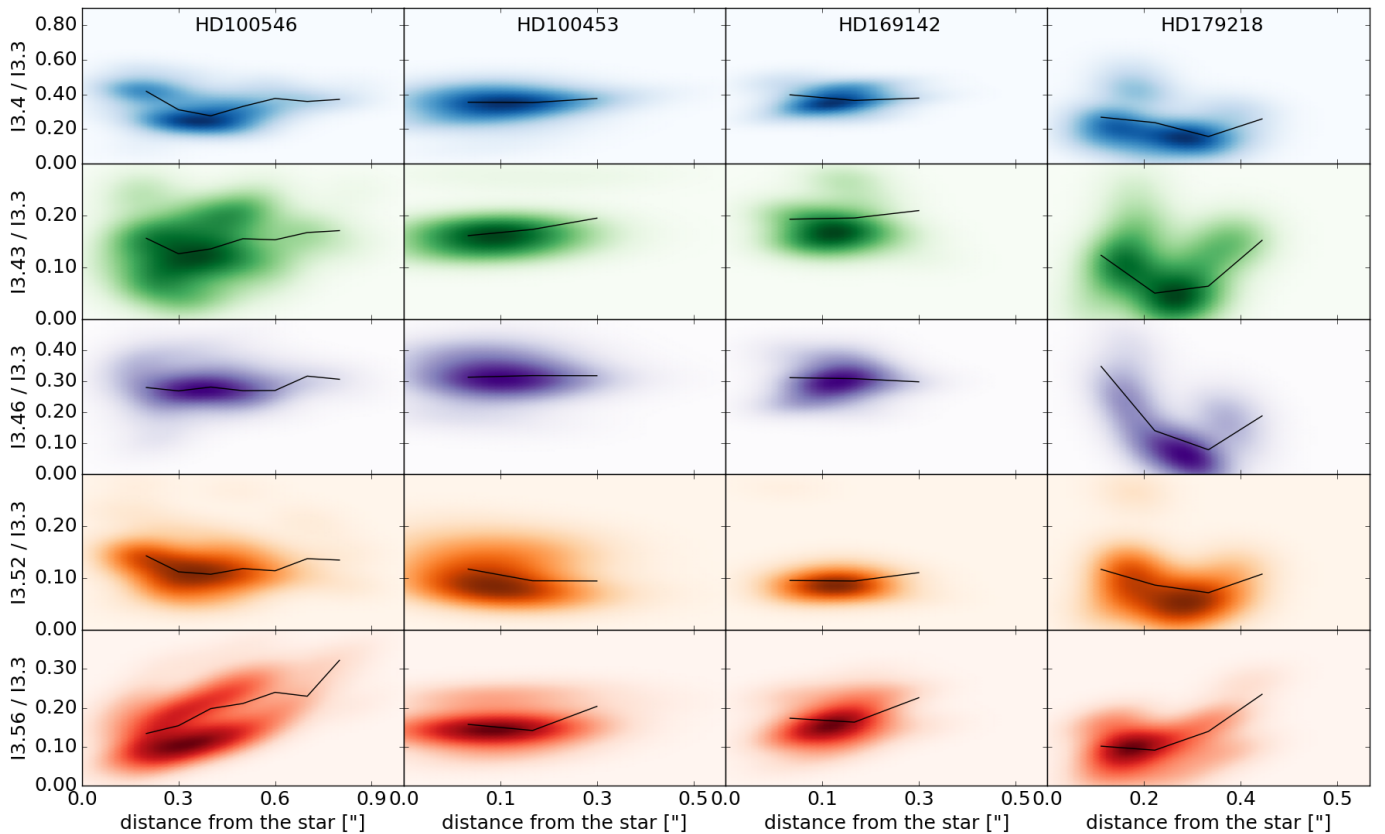


Fig. 5. Point densities are the band ratios (amplitude $\times \sigma$) of 3.4 (blue), 3.43 (green), 3.46 (magenta), 3.52 (orange), 3.56 (red) to the $3.3 \mu\text{m}$ versus the distance from the star. Densities of points are plotted rather than points to make the variations more visible. The median value of the ratio is plotted as black solid line.

$3.3 \mu\text{m}$ band evolution could thus be used as a diagnostic probe of the carbonaceous dust composition.

5.5. The 3.4 to $3.3 \mu\text{m}$ band ratio

The top panel in Fig. 5 shows values of the ratio between the 3.4 to $3.3 \mu\text{m}$ bands as a function of the distance from the star. Values of the averaged ratio are reported in Table 6. The ratio does not vary significantly with the distance while the radiation field intensity at the disk surface decreases by several orders of magnitude.

A previous study by Pilleri et al. (2015) focusing on spatially resolved spectra of the PDR NGC 7023 with AKARI and showed an increase in the 3.4 / $3.3 \mu\text{m}$ ratio when the FUV flux G_0 decreases. In order to make a comparison between our results with those of Pilleri et al. (2015), we applied our decomposition method (see Sect. 4) to their data to calculate the 3.4 / $3.3 \mu\text{m}$ ratio. We obtain higher ratios but they vary in the same way with G_0 as found by Pilleri et al. (2015) (Table 7).

Figure 7 shows the 3.4 / $3.3 \mu\text{m}$ ratio versus G_0 for NGC 7023 and the four disks. To calculate G_0 at different distances from the central star in disks, we have simply considered a blackbody with the effective temperature and stellar luminosity given in Table 2. The aliphatic-to-aromatic ratio does not appear to vary significantly between PDRs at the molecular edge and the disk surfaces. Assuming a constant gas density, with the orders of magnitude higher UV flux expected in our disk sample, with the Pilleri extrapolation, one would expect a very low 3.4/ $3.3 \mu\text{m}$ ratio, and a rapid dehydrogenation of the carriers following ex-

periments. However, the emission in the $3-4 \mu\text{m}$ range depends not only on the UV flux but also on the (re-)hydrogenation rate, which in turn depends on the gas density. Thus, the observation of an aliphatic-to-aromatic ratio that varies little may suggest either a recent exposure of the carriers to the radiation field (by a continuous local vertical replenishment at the disk surface) before their destruction/conversion, and/or that the ratio of G_0/n_H may be a better parameter to consider, and not the UV flux only. In disks, the gas density is expected to be much higher than in PDRs and must increase when we approach the star.

To go further in the understanding of the 3.4 / $3.3 \mu\text{m}$ ratio as a function of the local physical conditions, one can look at the intensity of the radiation in relation to the local gas density. Based on the model of Woitke et al. (2016) considering a disk in thermal and hydrostatical equilibrium, the gas density at the disk upper surface at the radial optical depth $A_v = 1$ can be estimated to be about $n_H = 10^9$ and 10^7 cm^{-3} respectively at 10 and 100 AU from the central star (see their Fig. 4 for their reference model). Thus, considering that G_0 scales as the inverse squared distance to the illuminating star, one can estimate that G_0 / n_H does not vary to first order between 10 and 100 AU. This could explain a 3.4 / $3.3 \mu\text{m}$ ratio that does not vary much with distance from the star in the disks. At the radial optical depth $A_v = 1$ and considering $G_0^{50 \text{ AU}}$ the FUV strength at 50 AU (see Table 2), one can roughly estimate the G_0 / n_H ratio as a function of the distance d from the star by $\sim G_0^{50 \text{ AU}} \times (\frac{50 \text{ AU}}{d})^2 \times e^{(-A_v=1)} / n_H(d)$. We find $G_0 / n_H \sim 0.04$ for HD 100546, ~ 0.002 and ~ 0.004 for HD 100453 and HD 169142 and ~ 0.15 for HD 179218 at 10 or 100 AU. The 3.4 / $3.3 \mu\text{m}$ ratios in HD 100546, HD 100453, and HD 169142, are comparable to those at the P2, P3, and P4 positions

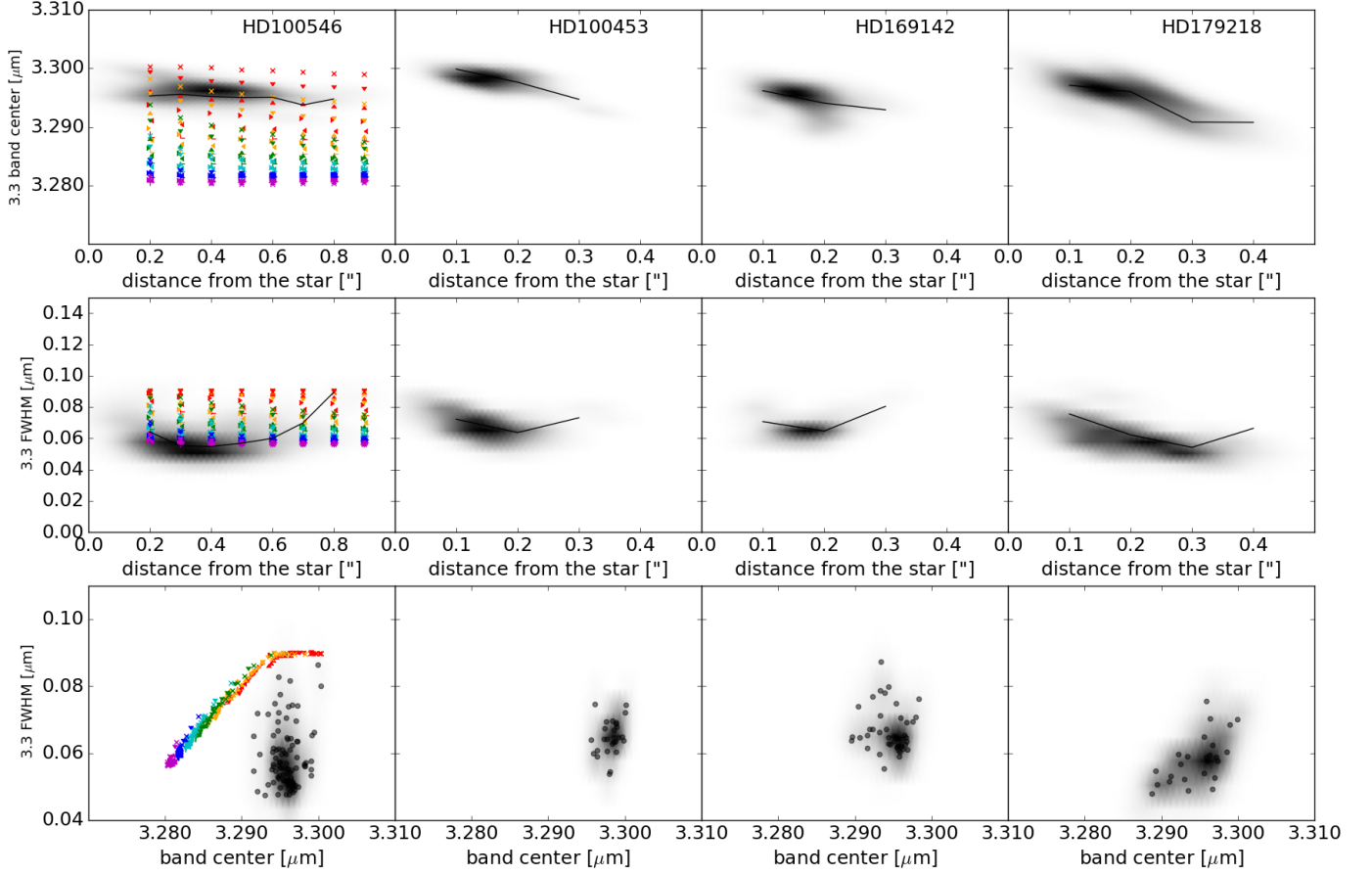


Fig. 6. In top panels, 3.3 μm band centre as a function of the distance from the star. In middle panels, 3.3 μm FWHM as a function of the distance from the star. In bottom panels, 3.3 μm FWHM over the band centre. For HD 100546, left panels, values are reported from THEMIS varying band gap from 0.1 eV (magenta) to 0.6 eV (red, as rainbow colours). Top two set of panel: Size increases bottom to top (for the same colour). Bottom panels: size increases from right to left.

Table 4. 3.3 μm band characteristics and variations as a function of the distance from the star (d).^a: too few data to calculate uncertainty.

HD 100546			HD 100453	
d ["]	λ_0 [μm]	FWHM [μm]	λ_0 [μm]	FWHM [μm]
0.1	--	--	3.300 ± 0.002	0.072 ± 0.008
0.2	3.295 ± 0.004	0.065 ± 0.011	3.298 ± 0.004	0.064 ± 0.006
0.3	3.296 ± 0.003	0.055 ± 0.005	3.294 ± 0.003	0.073 ± 0.005
0.4	3.295 ± 0.003	0.055 ± 0.007	3.293 ± 0.001	0.089 ± 0.000^a
0.5	3.295 ± 0.002	0.057 ± 0.008	--	--
0.6	3.295 ± 0.002	0.060 ± 0.012	--	--
0.7	3.294 ± 0.002	0.070 ± 0.010	--	--
0.8	3.295 ± 0.002	0.089 ± 0.013	--	--
0.9	3.295 ± 0.004	0.089 ± 0.002	--	--
HD 169142			HD 179218	
d ["]	λ_0 [μm]	FWHM [μm]	λ_0 [μm]	FWHM [μm]
0.1	3.296 ± 0.003	0.071 ± 0.010	3.297 ± 0.002	0.076 ± 0.012
0.2	3.294 ± 0.003	0.065 ± 0.004	3.296 ± 0.003	0.062 ± 0.012
0.3	3.293 ± 0.003	0.080 ± 0.009	3.291 ± 0.003	0.054 ± 0.003
0.4	3.294 ± 0.002	0.089 ± 0.000^a	3.291 ± 0.002	0.066 ± 0.007
0.5	--	--	3.290 ± 0.000^a	0.073 ± 0.000^a

in the PDR NGC 7023. In HD 179218, the 3.4 / 3.3 ratio is between that found for the P1 and P2 positions in the cavity and the PDR edge.

For NGC 7023, estimates of G_0 can be found in Pilleri et al. (2015) and of n_H (the total number of hydrogen nuclei) in Köhler et al. (2014). This gives: (i) $G_0/n_H = 10^2$ in the cavity (ionised

region - position P1); (ii) $G_0/n_H = 0.26\text{--}2.6$ at PDR's edge (position P2); (iii) $G_0/n_H = 1\text{--}2 \times 10^{-2}$ in the PDR ($A_V \sim 1$ - position P3); (iv) $G_0/n_H = 10^{-3}\text{--}2.5 \times 10^{-4}$ in the PDR ($A_V \sim 3$ - position P4). The 3.4 / 3.3 ratio is low in the cavity (P1) and remains constant toward the PDR even if G_0/n_H varies by several order of magnitudes. Combining the PDR and disks results, we find that

Table 5. Band centres, widths and variation ranges for each disk (d).

HD 100546		HD 100453		HD 169142		HD 179218	
λ_0 [μm]	FWHM [μm]	λ_0 [μm]	FWHM [μm]	λ_0 [μm]	FWHM [μm]	λ_0 [μm]	FWHM [μm]
3.394 ± 0.005	0.052 ± 0.006	3.391 ± 0.002	0.051 ± 0.004	3.389 ± 0.001	0.054 ± 0.001	3.390 ± 0.002	0.053 ± 0.004
3.430 ± 0.006	0.033 ± 0.008	3.432 ± 0.001	0.031 ± 0.003	3.431 ± 0.004	0.035 ± 0.004	3.432 ± 0.004	0.031 ± 0.007
3.468 ± 0.003	0.044 ± 0.007	3.469 ± 0.002	0.053 ± 0.004	3.470 ± 0.003	0.052 ± 0.004	3.469 ± 0.005	0.046 ± 0.008
3.515 ± 0.003	0.035 ± 0.007	3.520 ± 0.007	0.036 ± 0.008	3.515 ± 0.005	0.039 ± 0.007	3.516 ± 0.003	0.031 ± 0.004
3.560 ± 0.008	0.075 ± 0.013	3.561 ± 0.009	0.085 ± 0.006	3.562 ± 0.009	0.084 ± 0.009	3.569 ± 0.006	0.061 ± 0.018

Table 6. Ratios of the 3.4 to 3.3 μm bands for each disk. Their dispersion are also given.

	HD 100546	HD 100453	HD 169142	HD 179218
d ["]	3.4 / 3.3			
0.1	--	0.354 ± 0.122	0.397 ± 0.107	0.268 ± 0.165
0.2	0.418 ± 0.124	0.352 ± 0.068	0.365 ± 0.058	0.236 ± 0.121
0.3	0.311 ± 0.095	0.376 ± 0.058	0.378 ± 0.060	0.156 ± 0.085
0.4	0.276 ± 0.105	0.320 ± 0.029	0.418 ± 0.049	0.258 ± 0.053
0.5	0.330 ± 0.076	--	--	0.289 ± 0.000
0.6	0.376 ± 0.087	--	--	--
0.7	0.359 ± 0.041	--	--	--
0.8	0.371 ± 0.120	--	--	--
0.9	0.402 ± 0.076	--	--	--

Table 7. Ratios of the 3.4 to 3.3 μm bands for NGC 7023.

Position	G_0	3.4 / 3.3	
		Pilleri et al. (2015)	This work
P1	7000	0.028	0.181
P2	2600	0.090	0.318
P3	200	0.11	0.330
P4	150	0.13	0.336

the 3.4 / 3.3 ratio is roughly equal to 0.3 - 0.4 for $G_0/n_H \leq 10^{-2}$ while it decreases to ~ 0.2 for $G_0/n_H \geq 10^{-1}$.

In conclusion, the 3.4 / 3.3 band ratios observed in disks are comparable to those observed in PDRs and interestingly do not depend on the FUV strength over density ratio beyond a certain threshold. However, a more detailed study of the disk shape and irradiation conditions is needed to estimate more accurately the physical conditions (G_0 , n_H) at the disk surfaces. Specific radiative transfer code for each disk with the appropriate structure (cavities, gaps) would be required.

6. Modelling

The Heterogeneous dust Evolution Model for Interstellar Solids (THEMIS)¹ is based on data derived from laboratory experiments and is described in detail elsewhere (Jones 2012a,b,c; Jones et al. 2013; Köhler et al. 2014; Jones et al. 2017). THEMIS has been already used to analyse dense cloud observations (Köhler et al. 2015; Jones et al. 2016; Ysard et al. 2016), dust in the Magellanic Clouds (Chastenot et al. 2017) and other nearby galaxies within the Dustpedia project². Given that we are here mostly interested in the emission coming from stochastically-heated nano-particles we briefly summarise the essential elements pertaining to these particles of THEMIS, which have radii from 0.4 nm to several tens of nm, a power-law size distribution steeply declining in abundance with increasing radius.

¹ <https://www.ias.u-psud.fr/themis/>

² <http://dustpedia.com/>

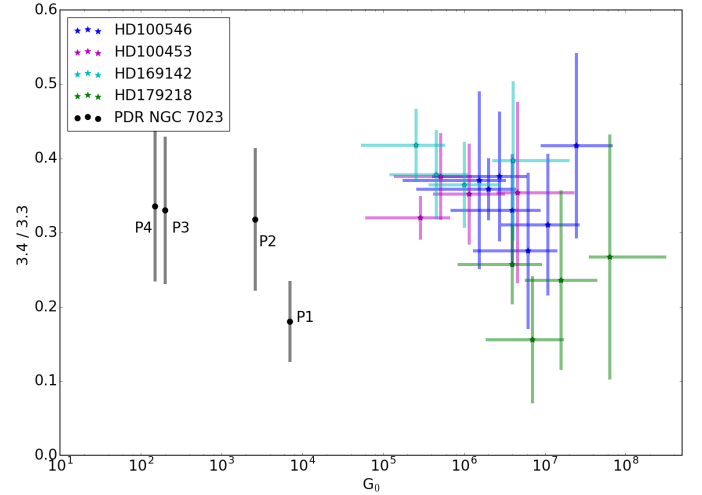


Fig. 7. 3.4 / 3.3 ratio as a function of G_0 . Black dot for band ratio in PDR NGC 7023 (based on Pilleri et al. (2015)). Stars for band ratio for each disk and different distances to the central star. For the disk, the G_0 has been estimated from a black body associated to the central star parameters (temperature and luminosity). Error bars for the 3.4 / 3.3 ratio are the dispersion of ratio values for the considered distance. Error bars for G_0 correspond to the values for the considered distance inside the VLT/NACO beam.

These nano-particles are primarily of amorphous, hydrogen-poor a-C composition and principally consist of poly-aromatic units linked together by olefinic/aliphatic bridges. These grains are rendered hydrogen-poor through the effects of photolytic dehydrogenation by the ambient interstellar UV radiation field in the diffuse ISM (Jones 2012a,b,c). The composition, structure and optical properties of the THEMIS carbonaceous grains, containing aromatic, olefinic and aliphatic sub-components are calculated using the extended random covalent network (eRCN) model for H-rich a-C:H and a defective graphite (DG) model for H-poor grains (Jones 2012a,b). The carbonaceous material properties are principally determined by their band gap with associ-

ated optical properties calibrated using the available laboratory data as described in detail in Jones (2012a,b).

For grains with radii ≤ 20 nm, the size of the aromatic clusters is necessarily limited. As derived in Robertson (1986), the band gap depends on the size of these clusters. Thus, for a given composition, the smaller grains will have a larger gap than their bulk counterpart (Jones 2012b,c). This last point is taken into account in THEMIS with the definition of an effective band gap, which depends upon the particle size. Thus, and in order to avoid any ambiguity in the following, we adopt the bulk material band gap in our description, with the advisory that, in general, the effective band gap is larger than the bulk material band gap (Jones 2012c).

In THEMIS the spectroscopic assignments for the C–H and C–C vibrational modes were based on the available laboratory spectroscopic data (Jones 2012a). The parametrized band characteristics are a compromise given the diversity encountered in laboratory data (see Fig. 1) and observed through the interstellar IR emission bands. Thus, the THEMIS IR spectral predictions are globally and qualitatively consistent with the observed laboratory and astronomical spectra. In particular, THEMIS can self-consistently explain the $3.3\ \mu\text{m}$ band and its associated side bands in the $3.4 - 3.6\ \mu\text{m}$ region. However, the current model is not able to explain the details of the observed emission spectra, *i.e.*, the band positions are not always in agreement with the observed bands and, as attested by the data presented in Fig. 1, neither are any of the available laboratory data sets. Thus, it appears that conditions in the laboratory cannot yet be made to match all the environments for the IR carriers in space and that is why we have not yet achieved completely satisfactory spectral fits of the models to the data. Additionally, the THEMIS model predictions were made for dust in the diffuse ISM, whereas the best IR emission band spectra are generally for PDR regions with generally more intense and harsher radiation fields.

In our exploration of the dust model parameter space, for a given disk as a function of distance, the THEMIS model grid contain almost 200 spectra which are calculated using DustEM³, a numerical tool for dust emission and extinction (Compiègne et al. 2011).

Using THEMIS in its current form we have calculated a model grid for each disk and explore the nature of the THEMIS nano-particles as a function of three parameters:

1. the distance from the star, which translates into the local radiation field expressed in terms of G_0 ,
2. the grain composition, in terms of the material effective band gap, E_g , which is explored over the range $E_g = 0.0 - 2.5$ eV, *i.e.*, from aromatic-rich materials ($E_g \sim 0$ eV) to aliphatic-rich, a-C:H like materials ($E_g > 2$ eV), and
3. variations in the minimum size of the carbonaceous nano-grain size distribution ranging from $a_{\min} = 0.4$ to 1.0 nm. For greater sizes, the distribution follow that of Jones et al. (2013).

Figure 8 shows an example of the wide variability in spectral energy distribution (SED) allowed by THEMIS. From the top left panel to the bottom right panel, the gap is increased, *i.e.*, underlying carriers vary from aromatic materials (low gap) to aliphatics (high gap). Increasing the gap leads to a switchover of the aromatic signature (black dashdot) at $3.3\ \mu\text{m}$ to olefins/aliphatics signatures (grey dashed/magenta dotted) between 3.4 and $3.6\ \mu\text{m}$ for higher gaps. On each panel color traces are SED with different minimal size of the smallest grains in

the distribution size and illustrates the prevalence of the surface or bulk effects. The emission properties of the smallest grains vary rapidly with size and in particular the band/continuum ratio. The choice of this range of minimum size allows to illustrate these variations. For small gaps, with increasing minimal size, we note an increase in the continuum emission and a decrease in the band emission due to both the surface/bulk effect and the effective lower gap for larger grains which are less limited by the size of aromatic clusters (Jones 2012a). For large gaps, as size increase, the continuum emission remains weak because the aromatic units are too small to allow emission at these wavelengths.

Thus, a first exploration is made through the grid to compare to the observations. We focus on HD 100546 which is the disk for which spectra cover the largest range of distances from the star. The radiation field was modelled by a black body with the temperature and luminosity of the central star, *i.e.* 10500 K and $32\ L_{\odot}$. The field intensity G_0 was calculated for step of $0.1''$ (star located at 103 pc). Thus, for each distance from the star, the SED is simulated for several sets of parameters of band gap E_g and minimal size a_{\min} . Then, to compare to the observations, the decomposition method presented in section 4 is used on the model data to get parameters of Gaussian functions. Model spectra are normalised to the observational spectrum at $0.2''$.

The results are presented in Fig. 9. Figs. B.1 and B.2 in appendix B show the comparison with other sets of parameters. In the left panel, results of the model decomposition are plotted (the similar aspect is due to the normalisation). On right panel, the relative intensities in the bands are reported on the same plot as in Fig. 4. For Fig. 9, where $a_{\min} = 0.5$ nm and $E_g = 0.1$ eV, we see that the intensities obtained after normalisation match the observations both in terms of relative order of distribution between the signatures for bands at 3.4 , 3.43 , 3.46 , and $3.52\ \mu\text{m}$ and in terms of intensities (derived from the field intensity G_0). When the a_{\min} varies from 0.5 to 0.4 nm (Fig. B.1), we observe a global shift to higher intensities. When the effective gap increases from 0.1 to 0.2 eV (with $a_{\min} = 0.5$ nm, Fig. B.2), intensities of aliphatic bands increase with respect to the $3.3\ \mu\text{m}$ band. The intensity of the signature at $3.56\ \mu\text{m}$ seems to be underestimated when we consider $a_{\min} = 0.5$ nm and $E_g = 0.1$ eV. As firstly seen in Sect. 5.1, the fit of the $3.56\ \mu\text{m}$ feature does not match very well. The decomposition method and THEMIS assume that observed signatures come from a-C:H materials that contain only carbon and hydrogen atoms. Thus, we speculate the $3.56\ \mu\text{m}$ feature could be explained by the chemical composition of the dust, such as inclusions of hetero-atoms of nitrogen or oxygen. Indeed, as reported by Tallent & Siewers (1956); Goebel et al. (1981), some carbonaceous materials with nitrogen or oxygen do have signatures around $3.56\ \mu\text{m}$. In the particular case of possible oxygen inclusion, some features expected in the mid-IR wavelength range may be searched for. With the inclusion of nitrogen in the aromatic network, this would be less evident as the infrared activity of potential new modes may be weak, but could influence and shift the position of some of the mid-IR aromatic modes (Socrates 2004).

Finally, as shown in Fig. 6 (bottom panel) in Sect. 5.4, we explore the width variation according to the band centre shift of the $3.3\ \mu\text{m}$ band. In THEMIS, both the increases in E_g (*i.e.* change in the grain composition) and a_{\min} drive the increase in the width and the shift of the band centre to longer wavelengths. This argues for multiple components for the $3.3\ \mu\text{m}$ band, from aromatic composition close to $3.28\ \mu\text{m}$ and hybrid aromatic-olefinic composition close to $3.30\ \mu\text{m}$.

³ <https://www.ias.u-psud.fr/DUSTEM/>

For the whole spectrum, we notice that the fit is not perfect. As explained above, THEMIS was developed for the diffuse ISM and signatures in this wavelength range present a great variability. Nevertheless, if the decomposition method does not use all signatures of the model, it fits signatures related to the same kind of materials (aliphatics) which evolve in a same way, as indicated by the correlation in Fig. 4. This first exploration allows us some interpretations of the dust composition and size. Keeping in mind that uncertainties remain high both on:

- radiation field intensity, due especially to the large spatial scale covered by one spectrum where G_0 varies quickly,
- analysis is based on averaged spectra for each distance and does not consider local variations due to the structure,

these results, by confirming that dust in HD 100546 is composed mostly of aromatic-rich sub-nanometer grains, with aliphatic and olefinic components, indicate that THEMIS is useful to model dust in disks and set limits on its composition and size. Nevertheless, a more detailed study has to be done to fully and definitively understand the observed variations and their origin.

7. Conclusions

We present NACO/VLT spectroscopic observations in the $3\ \mu\text{m}$ region of a small sample of HAeBe stars. These data allow us, for the first time, to spatially resolve the disk emission in the bands related to aromatic and aliphatic materials. Band assignments to aliphatic features is a complex question due to their high variability in terms of band positions and widths.

1. This work confirms the presence of features related to aromatic and aliphatic materials in disks around Herbig stars. These features are observed in a wide spatial range of the disks (from about ~ 10 to $100\ \text{au}$), even if the most inner parts of these disks remain inaccessible to our observations.
2. The various FUV radiation conditions and correlated intensities of aliphatic features with aromatic feature argue in favour of common nature of the carriers which are nano-grains stochastically heated. If there were distinct populations of carriers with significant different sizes, there would be no reason to have spatial correlated features.
3. No strong variations in band ratios (aliphatic / aromatic) according to the distance from the star are observed. This suggests features varying in a same way: same location, same intensity and argues for grains with mixed composition that is relatively stable. However, at a given distance, the dispersion of the values varies and depends on the data quality and the intrinsic decomposition variations but also on the physical dispersion due to the processes: aromatisation (due to UV irradiation), amorphisation, fragmentation and internal dynamics. An important point to consider is that the aliphatic bonds, more fragile than the aromatic rings, are expected to be the first to break under UV processing. Thus, no strong variation in aliphatic -aromatic band ratios suggests that a continuous replenishment at the disk surface would be at work. This is supported by the fact that nano-grains of comparable size are observed throughout the disks, whereas one would expect the smallest grains to be destroyed in the most irradiated areas. Photo-induced and/or collisional fragmentation of larger grains that may be important at the disk surfaces could be a possible process to explain the replenishment of the nano-grains component.

4. The 3.4/3.3 band ratios observed in disks are comparable to those observed in PDRs and appear to not only depend on the FUV strength but also on the gas density. Interestingly the 3.4 / 3.3 ratio does not depend on the FUV strength over density ratio beyond a certain threshold (of $G_0/n_H \leq 0.01$).
5. The band centre and FWHM variations in the $3.3\ \mu\text{m}$ band suggest multiple components of the feature with aromatic/olefinic composition. But evolution depends on the disk and remains unclear.
6. This first comparison with THEMIS gives a reasonable but not perfect match to the observations: this is not surprising since THEMIS was developed for the diffuse ISM.
7. The relative order of IR features are well reproduced with THEMIS for nano-grain population with $E_g = 0.1\ \text{eV}$ and $a_{\text{min}} = 0.5\ \text{nm}$.

This work raises new questions about the nature of the observed signatures and their underlying carriers. In our follow-up work we will characterise the processing times of dust grains at the disk surface (photo-dissociation, recombination, dehydrogenation) to understand the process of their replenishment. Regarding the detection of the bands and sub-bands of carbon dust in its many forms, which can be weak on a strong continuum, the combination of high spatial and spectral resolution, and sensitivity is essential. The forthcoming MATISSE/VLT and JWST observations will provide data that will allow us to further analyses and interpretations.

Acknowledgements. We thank our referee, A. Candian, for the care and quality of her comments and suggestions which greatly improved the clarity of this paper. This work was based on observations collected at the European Southern Observatory, Chile (ESO proposal number: 075.C-0624(A)) and was supported by P2IO LabEx (ANR-10-LABX-0038) in the framework "Investissements d'Avenir" (ANR-11-IDEX-0003-01) managed by the Agence Nationale de la Recherche (ANR, France), Programme National "Physique et Chimie du Milieu Interstellaire" (PCMI) of CNRS/INSU with INC/INP co-funded by CEA and CNES. We also acknowledge Paolo Pilleri for sharing his observations of the PDR NGC7023 (Pilleri et al. 2015).

References

- Acke, B., Bouwman, J., Juhász, A., et al. 2010, *The Astrophysical Journal*, 718, 558
- Acke, B. & van den Ancker, M. E. 2004, *Astronomy and Astrophysics*, 426, 151
- Acke, B. & Van den Ancker, M. E. 2006, *Astronomy & Astrophysics*, 449, 267
- Ardila, D. R., Golimowski, D. A., Krist, J. E., et al. 2007, *The Astrophysical Journal*, 665, 512
- Augereau, J. C., Lagrange, A. M., Mouillet, D., & Ménard, F. 2001, *Astronomy & Astrophysics*, 365, 78
- Benisty, M., Tatulli, E., Ménard, F., & Swain, M. R. 2010, *Astronomy & Astrophysics*, 511, A75
- Berné, O., Fuente, A., Pantin, E., et al. 2015, *Astronomy and Astrophysics*, 578, L8
- Bertrang, G. H.-M., Flock, M., & Wolf, S. 2017, *Monthly Notices of the Royal Astronomical Society*, 464, L61
- Biller, B. A., Males, J., Rodigas, T., et al. 2014, *The Astrophysical Journal Letters*, 792, L22
- Blades, J. C. & Whittet, D. C. B. 1980, *Monthly Notices of the Royal Astronomical Society*, 191, 701
- Boccaletti, A., Pantin, E., Lagrange, A.-M., et al. 2013, *Astronomy & Astrophysics*, 560, A20
- Bouwman, J., de Koter, A., Dominik, C., & Waters, L. B. F. M. 2003, *Astronomy & Astrophysics*, 401, 577
- Bouwman, J., Meeus, G., de Koter, A., et al. 2001, *Astronomy and Astrophysics*, 375, 950
- Brittain, S. D., Najita, J. R., & Carr, J. S. 2009, *The Astrophysical Journal*, 702, 85
- Brooke, T. Y., Tokunaga, A. T., & Strom, S. E. 1993, *The Astronomical Journal*, 106, 656

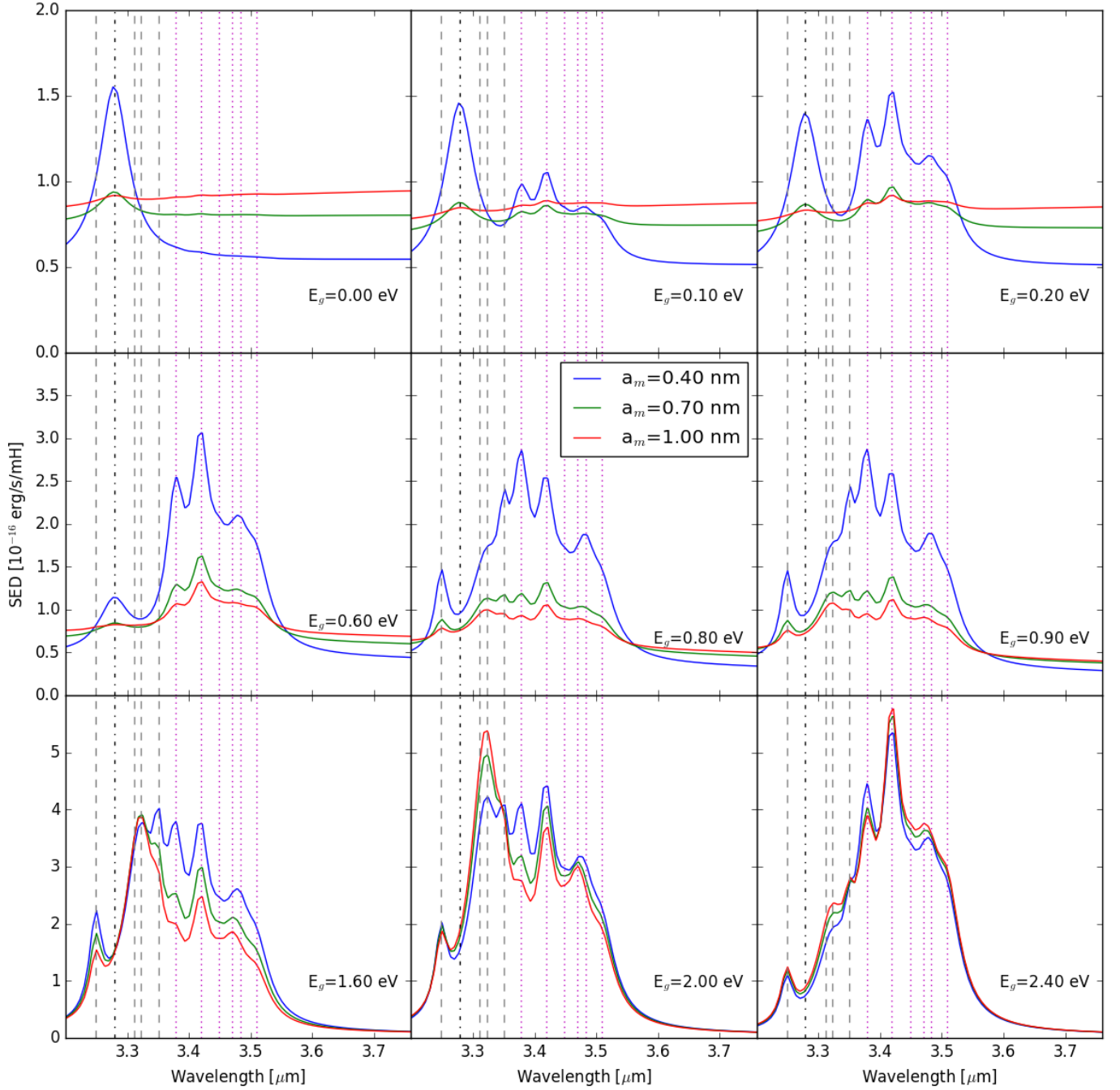


Fig. 8. SED in the 3.2-3.8 μm range calculated from THEMIS for a radiation field intensity $G_0 = 2.5 \times 10^7$ similar to that found in disks. Calculation made with DustEM. From top right to bottom left, band gap varies from 0.1 eV to 2.4 eV. In each subplot, SED is plotted for several minimal size of grains.

Candian, A., Kerr, T. H., Song, I.-O., McCombie, J., & Sarre, P. J. 2012, Monthly Notices of the Royal Astronomical Society, 426, 389
 Carpentier, Y., Féraud, G., Dartois, E., et al. 2012, Astronomy & Astrophysics, 548, A40
 Chastenet, J., Bot, C., Gordon, K. D., et al. 2017, Astronomy & Astrophysics, 601, A55
 Chen, C. H., Sargent, B. A., Bohac, C., et al. 2006a, The Astrophysical Journal Supplement Series, 166, 351
 Chen, X. P., Henning, T., van Boekel, R., & Grady, C. A. 2006b, Astronomy and Astrophysics, 445, 331
 Chiar, J. E., Tielens, A. G. G. M., Adamson, A. J., & Ricca, A. 2013, The Astrophysical Journal, 770, 78
 Collins, K. A., Grady, C. A., Hamaguchi, K., et al. 2009, The Astrophysical Journal, 697, 557
 Compiègne, M., Verstraete, L., Jones, A., et al. 2011, Astronomy and Astrophysics, 525, A103

Currie, T., Cloutier, R., Brittain, S., et al. 2015, The Astrophysical Journal Letters, 814, L27
 Dartois, E., Caro, G. M. M., Deboffle, D., Montagnac, G., & d'Hendecourt, L. 2005, Astronomy & Astrophysics, 432, 895
 Dartois, E., Marco, O., Muñoz-Caro, G. M., et al. 2004a, Astronomy & Astrophysics, 423, 549
 Dartois, E., Muñoz Caro, G. M., Deboffle, D., & d'Hendecourt, L. 2004b, Astronomy & Astrophysics, 423, L33
 Dischler, B. 1987, in: Proceedings of the EMRS Symposium, Vol. 17, 189
 Dominik, C., Dullemond, C. P., Waters, L. B. F. M., & Walch, S. 2003, Astronomy and Astrophysics, 398, 607
 Fedele, D., Carney, M., Hogerheijde, M. R., et al. 2017, Astronomy and Astrophysics, 600, A72
 Fedele, D., van den Ancker, M. E., Acke, B., et al. 2008, Astronomy and Astrophysics, 491, 809

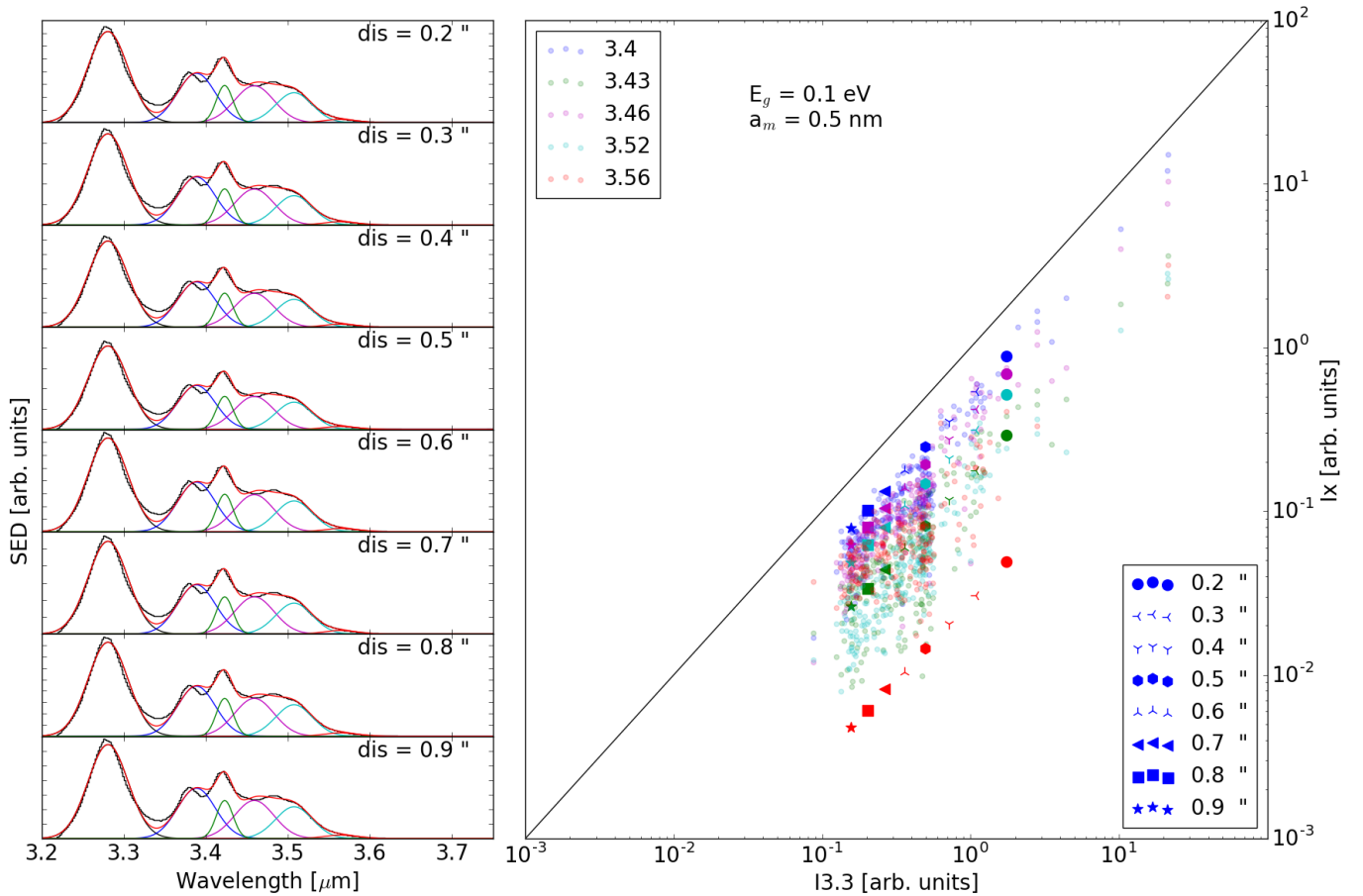


Fig. 9. In left panel, top down plots are the decomposition of the continuum subtracted spectra calculated with DustEM for a radial field intensity consistent with what is expected for HD 100546. All the spectra are normalised to the continuum at the distance at 0.2". In right panel, correlation between intensities in bands at 3.4, 3.43, 3.46, 3.52, 3.56 μm and the band at 3.3 μm underlined by those calculated for pixels of HD 100546 and previously shown in Fig. 4.

- Follette, K. B., Rameau, J., Dong, R., et al. 2017, arXiv:1704.06260 [astro-ph], arXiv: 1704.06260
- Furlan, E., Hartmann, L., Calvet, N., et al. 2006, The Astrophysical Journal Supplement Series, 165, 568
- Gaia Collaboration, Brown, A. G. A., Vallenari, A., et al. 2018, ArXiv e-prints, 1804, arXiv:1804.09365
- Garufi, A., Quanz, S. P., Schmid, H. M., et al. 2016, Astronomy & Astrophysics, 588, A8
- Geballe, T. R., Lacy, J. H., Persson, S. E., McGregor, P. J., & Soifer, B. T. 1985, The Astrophysical Journal, 292, 500
- Geers, V. C., Augereau, J.-C., Pontoppidan, K. M., et al. 2006, Astronomy and Astrophysics, 459, 545
- Geers, V. C., Pontoppidan, K. M., Van Dishoeck, E. F., et al. 2007a, Astronomy & Astrophysics, 469, L35
- Geers, V. C., van Dishoeck, E. F., Visser, R., et al. 2007b, Astronomy and Astrophysics, 476, 279
- Godard, M., Féraud, G., Chabot, M., et al. 2011, Astronomy & Astrophysics, 529, A146
- Goebel, J. H., Bregman, J. D., Witteborn, F. C., Taylor, B. J., & Willner, S. P. 1981, The Astrophysical Journal, 246, 455
- Goto, M., Gaessler, W., Hayano, Y., et al. 2003, \apj, 589, 419
- Goto, M., Henning, T., Kouchi, A., et al. 2009, The Astrophysical Journal, 693, 610
- Grady, C. A., Polomski, E. F., Henning, T., et al. 2001, The Astronomical Journal, 122, 3396
- Grady, C. A., Schneider, G., Hamaguchi, K., et al. 2007, The Astrophysical Journal, 665, 1391
- Guilloy, O., Ledoux, G., & Reynaud, C. 1999, The Astrophysical Journal Letters, 521, L133
- Habart, E., Natta, A., & Krügel, E. 2004, Astronomy & Astrophysics, 427, 179
- Habart, E., Natta, A., Testi, L., & Carillet, M. 2006, Astronomy & Astrophysics, 449, 1067
- Habing, H. J. 1968, Bulletin of the Astronomical Institutes of the Netherlands, 19, 421
- Hammonds, M., Mori, T., Usui, F., & Onaka, T. 2015, Planetary and Space Science, 116, 73
- Honda, M. 2013, Subaru Proposal, 1, 22
- Hu, J. Y., The, P. S., & de Winter, D. 1989, Astronomy and Astrophysics, 208, 213
- Joblin, C., Tielens, A., Allamandola, L. J., & Geballe, T. R. 1996, The Astrophysical Journal, 458, 610
- Jones, A. P. 1990, Monthly Notices of the Royal Astronomical Society, 247, 305
- Jones, A. P. 2012a, Astronomy and Astrophysics, 540, A1
- Jones, A. P. 2012b, Astronomy and Astrophysics, 540, A2
- Jones, A. P. 2012c, Astronomy and Astrophysics, 542, A98
- Jones, A. P., d'Hendecourt, L. B., Sheu, S.-Y., et al. 2004, Astronomy & Astrophysics, 416, 235
- Jones, A. P., Fanciullo, L., Köhler, M., et al. 2013, Astronomy & Astrophysics, 558, A62
- Jones, A. P., Köhler, M., Ysard, N., Bocchio, M., & Verstraete, L. 2017, arXiv:1703.00775 [astro-ph], arXiv: 1703.00775
- Jones, A. P., Köhler, M., Ysard, N., et al. 2016, Astronomy & Astrophysics, 588, A43
- Jourdain de Muizon, M., d'Hendecourt, L. B., & Geballe, T. R. 1990a, Astronomy and Astrophysics, 227, 526
- Jourdain de Muizon, M., d'Hendecourt, L. B., & Geballe, T. R. 1990b, Astronomy and Astrophysics, 235, 367
- Keller, L. D., Sloan, G. C., Forrest, W. J., et al. 2008, The Astrophysical Journal, 684, 411
- Khalafinejad, S., Maaskant, K. M., Mariñas, N., & Tielens, A. 2016, Astronomy & Astrophysics, 587, A62
- Klarman, L., Benisty, M., Min, M., et al. 2017, Astronomy and Astrophysics, 599, A80
- Kluska, J., Kraus, S., Davies, C. L., et al. 2018, The Astrophysical Journal, 855, 44
- Kraus, S., Ireland, M. J., Sitko, M. L., et al. 2013, The Astrophysical Journal, 768, 80

- Kwok, S. & Zhang, Y. 2011, *Nature*, 479, 80
- Köhler, M., Jones, A., & Ysard, N. 2014, *Astronomy & Astrophysics*, 565, L9
- Köhler, M., Ysard, N., & Jones, A. P. 2015, *Astronomy & Astrophysics*, 579, A15
- Lagage, P.-O., Doucet, C., Pantin, E., et al. 2006, *Science*, 314, 621
- Leger, A. & Puget, J. L. 1984, *Astronomy and Astrophysics*, 137, L5
- Li, A. & Lunine, J. I. 2003, *The Astrophysical Journal*, 594, 987
- Ligi, R., Vigan, A., Gratton, R., et al. 2017, 337–341
- Lindegren, L., Lammers, U., Bastian, U., et al. 2016, *Astronomy and Astrophysics*, 595, A4
- Liu, W. M., Hinz, P. M., Meyer, M. R., et al. 2003, *The Astrophysical Journal Letters*, 598, L111
- Long, Z. C., Fernandes, R. B., Sitko, M., et al. 2017, *The Astrophysical Journal*, 838, 62
- Maaskant, K. M., Honda, M., Waters, L. B. F. M., et al. 2013, *Astronomy and Astrophysics*, 555, A64
- Maaskant, K. M., Min, M., Waters, L., & Tielens, A. 2014, *Astronomy & Astrophysics*, 563, A78
- Malfait, K., Waelkens, C., Waters, L., et al. 1998, *Astronomy and astrophysics*, 332, L25
- Manoj, P., Bhatt, H. C., Maheswar, G., & Muneer, S. 2006, *The Astrophysical Journal*, 657
- Mariñas, N., Telesco, C. M., Fisher, R. S., & Packham, C. 2011, *The Astrophysical Journal*, 737, 57
- Meeus, G., Montesinos, B., Mendigutía, I., et al. 2012, *Astronomy and Astrophysics*, 544, A78
- Meeus, G., Salyk, C., Bruderer, S., et al. 2013, *Astronomy and Astrophysics*, 559, A84
- Meeus, G., Waters, L. B. F. M., Bouwman, J., et al. 2001, *Astronomy & Astrophysics*, 365, 476
- Mennella, V. 2008, *The Astrophysical Journal Letters*, 682, L101
- Menu, J., van Boekel, R., Henning, T., et al. 2015, *Astronomy and Astrophysics*, 581, A107
- Micelotta, E. R., Jones, A. P., & Tielens, A. G. G. M. 2010a, *Astronomy and Astrophysics*, 510, A37
- Micelotta, E. R., Jones, A. P., & Tielens, A. G. G. M. 2010b, *Astronomy and Astrophysics*, 510, A36
- Momose, M., Morita, A., Fukagawa, M., et al. 2015, *Publications of the Astronomical Society of Japan*, 67, 83
- Mulders, G. D., Min, M., Dominik, C., Debes, J. H., & Schneider, G. 2013, *Astronomy & Astrophysics*, 549, A112
- Muñoz Caro, G. M., Ruiterkamp, R., Schutte, W. A., Greenberg, J. M., & Mennella, V. 2001, *\aap*, 367, 347
- Osorio, M., Anglada, G., Carrasco-González, C., et al. 2014, *The Astrophysical Journal Letters*, 791, L36
- Panić, O., Ratzka, T., Mulders, G. D., et al. 2014, *Astronomy & Astrophysics*, 562, A101
- Peeters, E., Mattioda, A. L., Hudgins, D. M., & Allamandola, L. J. 2004, *The Astrophysical Journal Letters*, 617, L65
- Pilleri, P., Joblin, C., Boulanger, F., & Onaka, T. 2015, *Astronomy & Astrophysics*, 577, A16
- Pino, T., Dartois, E., Cao, A.-T., et al. 2008, *Astronomy & Astrophysics*, 490, 665
- Pirali, O., Vervloet, M., Dahl, J. E., et al. 2007, *The Astrophysical Journal*, 661, 919
- Pohl, A., Benisty, M., Pinilla, P., et al. 2017, *The Astrophysical Journal*, 850, 52
- Quanz, S. P., Amara, A., Meyer, M. R., et al. 2015, *The Astrophysical Journal*, 807, 64
- Quanz, S. P., Avenhaus, H., Buenzli, E., et al. 2013, *The Astrophysical Journal Letters*, 766, L2
- Reggiani, M., Quanz, S. P., Meyer, M. R., et al. 2014, *The Astrophysical Journal Letters*, 792, L23
- Ristein, J. 1998, *Journal of Applied Physics*, 84, 3836
- Roberts, K. R. G., Smith, K. T., & Sarre, P. J. 2012, *Monthly Notices of the Royal Astronomical Society*, 421, 3277
- Robertson, J. 1986, *Advances in Physics*, 35, 317
- Sadjadi, S., Zhang, Y., & Kwok, S. 2017, arXiv:1707.07415 [astro-ph], arXiv: 1707.07415
- Schworer, G., Lacour, S., Huélamo, N., et al. 2017, *The Astrophysical Journal*, 842, 77
- Schütz, O., Meeus, G., & Sterzik, M. F. 2005, *Astronomy and Astrophysics*, 431, 165
- Seok, J. Y. & Li, A. 2016, *The Astrophysical Journal*, 818, 2
- Seok, J. Y. & Li, A. 2017, *The Astrophysical Journal*, 835, 291, arXiv: 1612.09454
- Sheu, S.-Y., Lee, I.-P., Lee, Y. T., & Chang, H.-C. 2002, *The Astrophysical Journal Letters*, 581, L55
- Sloan, G. C., Bregman, J. D., Geballe, T. R., Allamandola, L. J., & Woodward, C. E. 1997, *\apj*, 474, 735
- Sloan, G. C., Keller, L. D., Forrest, W. J., et al. 2005, *The Astrophysical Journal*, 632, 956
- Socrates, G. 2004, *Infrared and Raman Characteristic Group Frequencies: Tables and Charts* (John Wiley & Sons), google-Books-ID: LDoAAjMnwEIC
- Song, I.-O., Kerr, T. H., McCombie, J., & Sarre, P. J. 2003, *Monthly Notices of the Royal Astronomical Society*, 346, L1
- Taha, A. S., Labadie, L., Pantin, E., et al. 2018, *Astronomy & Astrophysics*, 612, A15
- Tallent, W. H. & Siewers, I. J. 1956, *Analytical Chemistry*, 28, 953
- Tatulli, E., Benisty, M., Ménard, F., et al. 2011, *Astronomy & Astrophysics*, 531, A1
- Tokunaga, A. T., Sellgren, K., Smith, R. G., et al. 1991, *The Astrophysical Journal*, 380, 452
- van Boekel, R., Min, M., Waters, L. B. F. M., et al. 2005, *Astronomy and Astrophysics*, 437, 189
- van der Plas, G., van den Ancker, M. E., Acke, B., et al. 2009, *Astronomy and Astrophysics*, 500, 1137
- Van Kerckhoven, C., A. G. G. M Tielens, & Waelkens, C. 2002, *Astronomy & Astrophysics*, 384, 568
- vanBoekel, R., M.Waters, L. B. F., Dominik, C., et al. 2004, *Astronomy & Astrophysics*, 418, 177
- Wagner, K. R., Daniel, A., & Kasper, M. 2017, in , 4028
- Woitke, P., Min, M., Pinte, C., et al. 2016, *Astronomy & Astrophysics*, 586, A103
- Yang, X. J., Glaser, R., Li, A., & Zhong, J. X. 2013, *The Astrophysical Journal*, 776, 110
- Yang, X. J., Li, A., Glaser, R., & Zhong, J. X. 2016, *The Astrophysical Journal*, 825, 22
- Ysard, N., Köhler, M., Jones, A., et al. 2016, *Astronomy and Astrophysics*, 588, A44

Appendix A: disks

Appendix A.1: HD 100546

HD 100546 is one of the nearest very well studied Herbig Be stars ($d=109\pm4$ pc [Gaia Collaboration et al. 2018](#); [Lindgren et al. 2016](#)). Based on HST and ground-based high-contrast images, an elliptical structure are detected and extended up to 350–380 AU ([Augereau et al. 2001](#)) and multiplied-armed spiral patterns are identified ([Grady et al. 2001](#); [Ardila et al. 2007](#); [Boccaletti et al. 2013](#)). An inner dust disk extending from ~ 0.2 AU to ~ 1 –4 AU was resolved using near-IR interferometry ([Benisty et al. 2010](#); [Tatulli et al. 2011](#); [Mulders et al. 2013](#); [Panić et al. 2014](#)). The (pre-)transitional nature of HD 100546 was initially proposed by [Bouwman et al. \(2003\)](#) from a SED analysis. The presence of a gap extending up to 10–15 AU has been confirmed from mid-IR interferometry ([Liu et al. 2003](#); [Panić et al. 2014](#)), spectroscopy in the UV and the near-IR ([Grady et al. 2007](#); [Brittain et al. 2009](#); [van der Plas et al. 2009](#)), and high-resolution polarimetric imaging in the optical and near-IR ([Quanz et al. 2015](#); [Garufi et al. 2016](#); [Follette et al. 2017](#)).

It is the first disk in which crystalline silicates ([Hu et al. 1989](#)) and aromatic bands ([Malfait et al. 1998](#)) have been detected. HD100546 is one of the few HAeBe stars to show, at the same time, strong aromatic bands luminosity and warm gas lines luminosities ([Meeus et al. 2012, 2013](#)). The 8.6 and 11.3 μm aromatic features are spatially extended on a few 100 AU scale ([vanBoekel et al. 2004](#)), and the spatial distribution of the 3.3 μm emission shows a gap in the innermost region (~ 5 –10 AU) and is extended up to at least 50 AU ([Habart et al. 2006](#)). The FWHM is about $\sim 12 \pm 3$ AU [Geers et al. \(2007b\)](#). In [Habart et al. \(2006\)](#), some additional features in the 3.4–3.5 μm region are also detected, that are at the time attributed to aliphatic C-H stretches in methyl or ethyl side-groups attached to PAHs ([Joblin et al. 1996](#); [Yang et al. 2013, 2016](#)) or nano-diamonds.

Appendix A.2: HD 100453

The Herbig Ae star HD 100453A ($d=104\pm3$ pc, $M = 1.7M_{\text{sol}}$ [Gaia Collaboration et al. 2018](#); [Dominik et al. 2003](#)), is less brighter and studied than HD 100546. Whose proto-planetary disk was recently revealed to host a gap ([Khalafinejad et al. 2016](#)) and a global two-armed spiral structure in SPHERE/VLT image consistent with a companion-driven origin ([Wagner et al. 2017](#)) [and reference therein]. The primary A-star hosts an M-dwarf companion with a mass of $\sim 0.2M$ and an angular separation of 1.05", corresponding to a projected physical separation of ~ 108 AU if the orbit is seen close to face-on ([Chen et al. 2006b](#); [Collins et al. 2009](#)). The spatially resolved MIR Q-band image obtained with Gemini north/MICHELLE indicates an outer gap edge at ~ 20 AU and the disk is extended up to ~ 200 AU ([Khalafinejad et al. 2016](#)). From Gemini Planet Imager (GPI) polarized intensity (PI), SPHERE data and the IR SED fitting, [Long et al. \(2017\)](#) suggests that the circumstellar disk of HD 100453 appears to contain an inner disk which SED fitting suggests extends from 0.13 - 1 AU, followed by a large radial gap (1 - 18 AU), and an outer disk (18 - 39 AU).

Its Spitzer/IRS spectrum showing a very weak sign of silicate features at 10 and 20 μm indicates also the presence of a gap in the disk (e.g. [Mariñas et al. 2011](#); [Maaskant et al. 2013](#)). The aromatic feature at 3.3, 6.2, 7.8, 8.6, 11.3 and 12.7 μm are detected ([Meeus et al. 2001](#)), with secondary features observed at 5.7, 6.0, 10.6, 12.0, and 13.5 μm , and the 6.8 and 7.2 μm aliphatic bands ([Acke et al. 2010](#)). HD 100453 also displays an emission

feature at 16–19 μm , that could be attributed to the out-of-plane skeletal modes of large elongated PAH molecules ([Peeters et al. 2004](#); [Acke et al. 2010](#)). The 3.3 μm aromatic feature is spatially extended with a FWHM equal to ~ 20 AU ([Habart et al. 2006](#); [Klarmann et al. 2017](#)) presents NIR Interferometric observations showing extended flux that could be evidence for carbonaceous stochastically heated particles in the inner region of the proto-planetary disks around HD 100453.

Appendix A.3: HD 169142

HD 169142 is a Herbig Ae star (A5Ve; [Keller et al. 2008](#)), well-studied at a distance of 117 ± 4 pc ([Grady et al. 2007](#); [Manoj et al. 2006](#); [Gaia Collaboration et al. 2018](#)). It shows an (almost face-on) disk with (i) multiple gaps (an inner between ~ 1 and ~ 20 AU and a middle between ~ 30 and ~ 55 AU) (ii) dust rings at the edge of the gaps (at ~ 20 –30 AU and at 55–85 AU) and (iii) an outer disk (e.g. [Honda 2013](#); [Quanz et al. 2013](#); [Osorio et al. 2014](#); [Momose et al. 2015](#); [Fedele et al. 2017](#); [Ligi et al. 2017](#); [Bertrang et al. 2017](#)).

[Seok & Li \(2016\)](#); [Pohl et al. \(2017\)](#) also model dust population according to its location or its evolution. [Seok & Li \(2016\)](#) performed a comprehensive modeling of its SED as well as the PAH emission features with porous dust and astronomical-PAHs and found that three dust populations and relatively small PAH molecules with an ionization fraction of 0.8 can explain the entire SED and the observed PAH features⁴. In this disk, the aromatic feature at 3.3 μm is clearly detected with the other aromatic bands 6.2, 7.8, 8.6, 11.3 and 12.7 μm ([Meeus et al. 2001](#); [Sloan et al. 2005](#)), as well as, secondary features observed at 5.7, 6.0, 10.6, 12.0, and 13.5 μm , and the 6.8 and 7.2 μm aliphatic bands ([Acke et al. 2010](#)). The 3.3 μm aromatic feature appears to be observed in the inner cavity and is spatially extended with a FWHM of 0.3" or ~ 30 AU ([Habart et al. 2006](#), and this paper).

Appendix A.4: HD 179218

HD 179218 is at a distance of ~ 290 pc ([Gaia Collaboration et al. 2018](#)) with a B9 spectral type and a strong luminosity of $\sim 180 L_{\odot}$. It harbors a circumstellar disk revealed through its IR excess and that is well known for its silicates dominated IR spectrum ([Bouwman et al. 2001](#); [Schütz et al. 2005](#); [van Boekel et al. 2005](#)). Its IR spectra are dominated by crystalline forsterite and enstatite rather than small, amorphous silicate grains, HD 179218 is known to have a large percentage of crystalline dust. This indicates dust processing in the circumstellar disk of HD 179218, and the presence of cold enstatite at ~ 10 AU implies that enstatite is mostly produced in the inner regions and is transported outward by radial mixing ([van Boekel et al. 2005](#)). A double-ring-like emission at 10 μm has been spatially resolved HD 179218 is at a distance of ~ 290 pc (e.g., [Fedele et al. 2008](#)), peaking at ~ 1 and 20 AU, respectively. A gap at ~ 10 AU is reported based on the MIR interferometry with VLT/MIDI HD 179218 is at a distance of ~ 290 pc ([Menu et al. 2015](#)).

The aromatic feature at 3.3 μm is detected, as well as, the other aromatic bands at 6.2, 7.8 and 8.6 μm ([Meeus et al. 2001](#); [Acke & van den Ancker 2004](#); [Acke et al. 2010](#)). A very recent study HD 179218 is at a distance of ~ 290 pc ([Taha et al. 2018](#)) has had for the first time spatially resolved aromatic emission of

⁴ Similar PAHs properties are derived by [Seok & Li](#) for HD100453 and HD 179218, while for HD100546 relatively large PAHs with a small ionization fraction are found. The ionization fraction is the probability of finding a PAH molecule in a nonzero charge state ([Li & Lunine 2003](#))

the disk. The average FWHM of the 8.6 and 11.3 μm is of 0.232" or 67 AU and 0.280" or 81 AU. Based on spatial and spectroscopic considerations as well as on qualitative comparison with IRS 48 and HD 97048, they favor a scenario in which PAHs extend out to large radii across the flared disk surface and are at the same time predominantly in an ionized charge state due to the strong UV radiation field of the central star. The 3.3 μm aromatic feature is detected from 0.1" until 0.5" or 150 AU from the central star. In this study, we find that the FWHM is about 0.2" or ~ 60 AU. Kluska et al. (2018) presents NIR Interferometric observations showing extended flux that could be evidence for carbonaceous stochastically heated particles in the inner region of the proto-planetary disks around HD 179218.

Appendix B: Comparison THEMIS with observations

Figures B.1 and B.2 show correlations between the aliphatic bands and the aromatic one for two sets of parameters with THEMIS : ($E_g=0.2$ eV, $a_{\text{min}}=5$ nm) and ($E_g=0.1$ eV, $a_{\text{min}}=4$ nm), respectively. See Sec. 6 for details

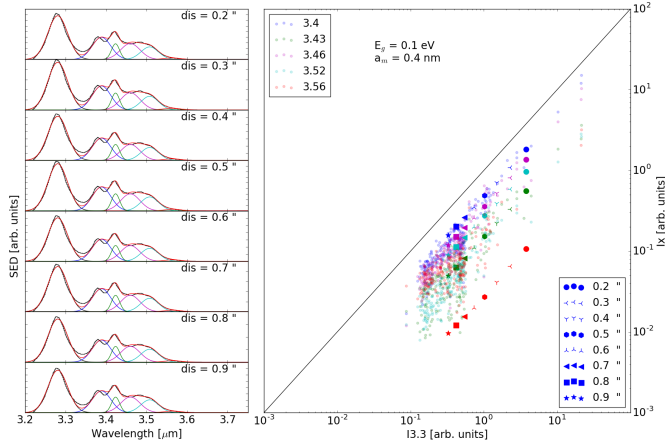


Fig. B.1. This figure shows the correlation between intensities in bands 3.4, 3.43, 3.46, 3.52, 3.46 and the band at 3.3 μm underlined by those calculated for pixels of HD 100546 and previously shown in Fig. 4.

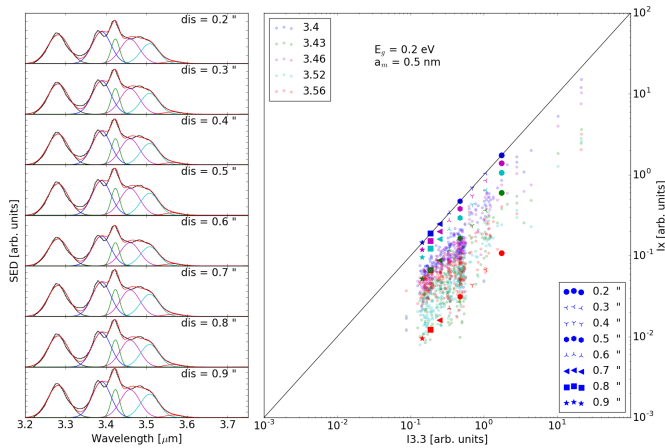


Fig. B.2. This figure shows the correlation between intensities in bands 3.4, 3.43, 3.46, 3.52, 3.46 and the band at 3.3 μm underlined by those calculated for pixels of HD 100546 and previously shown in Fig. 4.